AGU PUBLICATIONS

JGR

Journal of Geophysical Research: Planets

RESEARCH ARTICLE
10.1002/2014JE004658

Key Points:
- Small craters on Meridiani Planum vary in age from <50–200 ka to ~20 Ma
- The decrease in degradation rate can be explained by topographic diffusion
- Erosion rates on Mars indicate a wet climate >3 Ga followed by a dry environment

Supporting Information:
- Readme
- Tables S1a and S1b
- Text S1
- Table S2

Correspondence to:
M. P. Golombek,
mgolombek@jpl.nasa.gov

Citation:
Golombek, M. P., N. H. Warner, V. Ganti, M. P. Lamb, T. J. Parker, R. L. Fergason, and R. Sullivan (2014), Small crater modification on Meridiani Planum and implications for erosion rates and climate change on Mars, *J. Geophys. Res. Planets*, *119*, doi:10.1002/2014JE004658.

Received 29 APR 2014
Accepted 4 NOV 2014
Accepted article online 10 NOV 2014

Small crater modification on Meridiani Planum and implications for erosion rates and climate change on Mars

M. P. Golombek[1], N. H. Warner[1,2], V. Ganti[3], M. P. Lamb[3], T. J. Parker[1], R. L. Fergason[4], and R. Sullivan[5]

[1]Jet Propulsion Laboratory, California Institute of Technology, Pasadena, California, USA, [2]Department of Geological Sciences, State University of New York College at Geneseo, Geneseo, New York, USA, [3]Division of Geological and Planetary Sciences, California Institute of Technology, Pasadena, California, USA, [4]Astrogeology Science Center, U.S. Geological Survey, Flagstaff, Arizona, USA, [5]Department of Astronomy, Cornell University, Ithaca, New York, USA

Abstract A morphometric and morphologic catalog of ~100 small craters imaged by the *Opportunity* rover over the 33.5 km traverse between Eagle and Endeavour craters on Meridiani Planum shows craters in six stages of degradation that range from fresh and blocky to eroded and shallow depressions ringed by planed off rim blocks. The age of each morphologic class from <50–200 ka to ~20 Ma has been determined from the size-frequency distribution of craters in the catalog, the retention age of small craters on Meridiani Planum, and the age of the latest phase of ripple migration. The rate of degradation of the craters has been determined from crater depth, rim height, and ejecta removal over the class age. These rates show a rapid decrease from ~1 m/Myr for craters <1 Ma to ~ <0.1 m/Myr for craters 10–20 Ma, which can be explained by topographic diffusion with modeled diffusivities of ~10^{-6} m^2/yr. In contrast to these relatively fast, short-term erosion rates, previously estimated average erosion rates on Mars over ~100 Myr and 3 Gyr timescales from the Amazonian and Hesperian are of order <0.01 m/Myr, which is 3–4 orders of magnitude slower than typical terrestrial rates. Erosion rates during the Middle-Late Noachian averaged over ~250 Myr, and ~700 Myr intervals are around 1 m/Myr, comparable to slow terrestrial erosion rates calculated over similar timescales. This argues for a wet climate before ~3 Ga in which liquid water was the erosional agent, followed by a dry environment dominated by slow eolian erosion.

1. Introduction

The *Opportunity* rover has traversed over 38 km across Meridiani Planum and has spent most of that time (>10 years) traveling to large craters or imaging smaller ones along the way (Figure 1). Large craters have been targets because they provide access to cross sections of sandstones that underlie most of the plains. As a result, the most intensive investigations of these rocks have been at Eagle crater (56 sols; sols = Martian solar days = 24.6 h) where *Opportunity* landed, at Endurance crater (219 sols) where *Opportunity* sampled Burns formation strata on the interior wall, and at Victoria crater (729 sols) where *Opportunity* documented a stratigraphic section within the floor of Duck Bay [*Squyres et al*., 2006; *Arvidson et al*., 2011]. After Victoria, *Opportunity* traversed about 20 km to reach the rim of Endeavour crater to sample older Noachian rocks preserved in the eroded rim [*Squyres et al*., 2012; *Arvidson et al*., 2014].

Opportunity has imaged about 100 smaller craters during its traverse, in addition to traversing to large craters to investigate the outcrop exposures. Some of these were targets of opportunity in which images were acquired during short middrive stops by rover cameras in "drive by shootings," whereas others (e.g., Resolution cluster, Concepción, and Santa Maria) were identified in orbital images and specifically chosen as waypoints. Most of these craters are relatively small, 5–30 m in diameter, and they are located in portions of Meridiani Planum with different terrain. The first portion of the traverse occurred on a low-relief sandy surface with very small ripples (cm high) and almost no outcrop (Figures 2 and 3). As *Opportunity* traversed south from Endurance the ripples became larger (meter high) and outcrop became more common. After getting stuck in Purgatory ripple (65 sols), north of Erebus, ripples were large enough that extreme care was used in selecting drive paths in troughs between them. The traverse from the edge of the Victoria annulus to Endeavour deviated dramatically from the shortest path to avoid very large ripples that could have embedded the rover. Finally, the last third of the traverse was on smoother sandy and low-relief outcrop

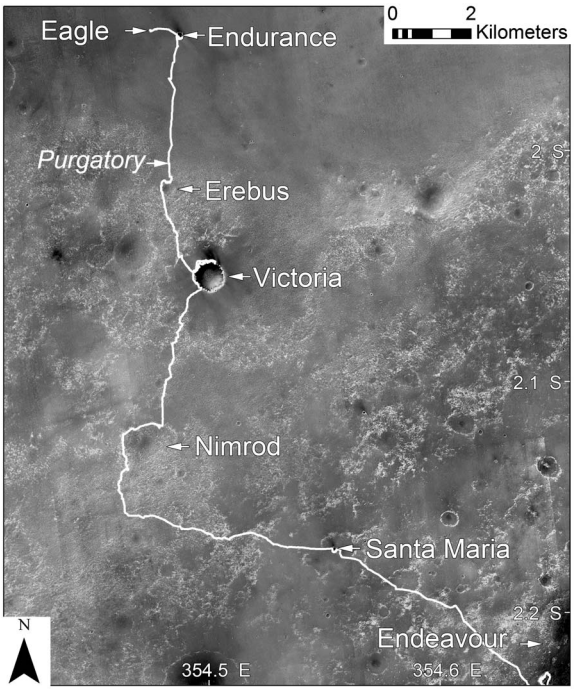

Figure 1. HiRISE image of *Opportunity's* 33.5 km traverse across Meridiani Planum showing major craters along route and the different terrains. Mosaic was compiled from 12 HiRISE map-projected images at 25 cm/pixel progressively georeferenced to CTX and MOLA and incorporated into mission planning software for localization and traverse planning [*Parker et al.*, 2010, 2012].

terrain. The numbers of craters encountered in different portions of the traverse can be related to the surface terrain (Figure 2).

The small craters imaged by *Opportunity* are in a wide variety of morphologic states. Previous investigations of craters on Meridiani Planum from field observations by the *Opportunity* rover and high-resolution images have documented a sequence of modification that has proceeded from fresh blocky craters to highly eroded and shallow depressions ringed by planed off crater rim outcrop blocks [*Grant et al.*, 2006a; *Golombek et al.*, 2006a, 2010; *Golombek*, 2012]. This degradation sequence is produced by abrasion and infilling from abundant basaltic sand that has effectively smoothed the topography. Rover observations have documented that the sandstones are very susceptible to erosion and that blocks of ejecta are planed off parallel to the sand surface and the ubiquitous granule ripples. Spherical erosionally resistant concretions that are millimeters in diameter, called blueberries, have weathered out of the Burns formation sulfate-rich sandstones and armor the ripples [*Soderblom et al.*, 2004; *Squyres et al.*, 2006].

Because small impact craters have a well-understood initial geometry (depth, rim height, and ejecta block size) that is directly related to their diameter [*Pike*, 1977; *Melosh*, 1989], simple morphometric measurements of craters can be used to measure changes from when they first formed. Crater counts have determined a very young average crater retention age of $<$20 Ma for Meridiani Planum craters $<$250 m diameter [*Lane et al.*, 2003]. Subsequent observations of craters that are younger and older than the granule ripples by the *Opportunity* rover and in HiRISE (High-Resolution Imaging Science Experiment) images have constrained the latest phase of granule ripple migration to have occurred between ~50 and ~200 ka [*Golombek et al.*, 2010]. As a result, the morphologic and degradational state of the craters along with their interaction with ripples can be used to construct a timescale for their formation and modification based on crater retention ages for all small craters, those younger than ripple migration, and those at various stages of modification in between.

We begin this paper with a description of the *Opportunity* traverse across Meridiani Planum, including the terrains it covered, to place the craters observed into context. Next a complete catalog of all craters observed by *Opportunity* from landing at Eagle crater to the Endeavour rim is described. From this catalog, the degradational state and morphological classification scheme is described. Next we develop a timescale for crater formation and modification and from that determine the rate of crater modification. Results are discussed in terms of the rate of erosion and degradation through time and compared to long-term erosion rates calculated for Meridiani Planum and Mars in general. This paper also includes three supporting information files. The first supporting information file is the complete crater catalog in a table with crater name, sol imaged, diameter, depth, morphology, morphologic class, age and degradation rate arranged by the order of exploration (Table S1a) and in alphabetical order by crater name (Table S1b). The second is a more complete historical description of the *Opportunity* rover traverse from Eagle to Endurance crater that includes details on traverse planning, science operations and localization (Text S1). Finally, the third is a table of crater diameter (square root of 2 bins), number of craters, and age from incremental size-frequency distribution of class 1–6 craters in the catalog imaged by the *Opportunity* rover on Meridiani Planum that includes highlighted diameters showing the bins used for making the resurfacing correction as described in the text (Table S2).

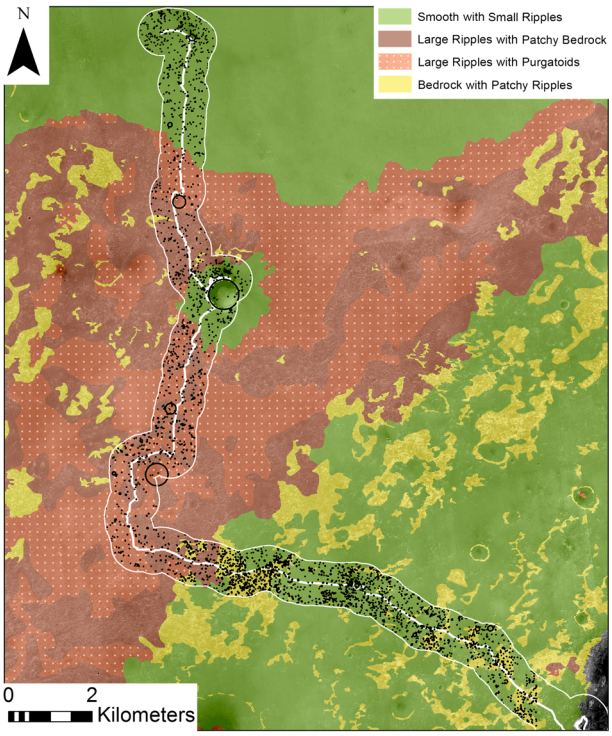

Figure 2. Map of different terrains and craters counted in HiRISE within 500 m on each side of the rover traverse. Area is the same as Figure 1.

2. The *Opportunity* Traverse

The *Opportunity* rover has traversed over 40 km across Meridiani Planum in over 10 years (Figure 1 and Text S1 in the supporting information). After landing in Eagle crater and exploring exposures of sulfate-rich sandstones of the Burns formation, *Opportunity* exited the crater on Sol 56 and traversed about 700 m to the east (Figure 4) to Endurance crater (150 m diameter) [*Squyres et al.*, 2006]. The plains between Eagle and Endurance appeared smooth in available Mars Orbiter Camera (MOC) images [*Malin et al.*, 2010], and *Opportunity* traversed across an exceptionally flat sandy surface with relatively sparse centimeter-sized ripples.

After exploring the inner rim of Endurance crater (Sols 131–316) the rover began a roughly 6 km traverse from Endurance crater to Victoria crater to the south (Figure 4), with a planned stop at the backshell along the way (Sols 324–357) [*Squyres et al.*, 2006]. During the drive south, a series of craters (Argo, Alvin, Jason, Naturaliste, Gauss, Vostock, James Caird, Nina, Vega, Viking, and Voyager) were used as imaging targets (Table S1a) and as navigation tools (via triangulation).

Initially the terrain south of Endurance was almost as smooth, flat, and sandy as that between Eagle and Endurance craters (Figure 4), but after about 3 km, the ripples to the south became larger (several meters wide and tens of centimeters high). Most of the ripples encountered trended north-south and were armored by blueberry granules, but cross drifts of very fine sand trending northeast-southwest also became more common. On Sol 446, *Opportunity's* wheels became embedded in such a cross drift named Purgatory ripple [*Squyres et al.*, 2006; *Arvidson et al.*, 2011].

After Purgatory ripple, most drives were planned along firm troughs between granule ripples or on exposures of outcrop (Figure 4). On Sol 590, *Opportunity* came upon the north rim of the 330 m diameter very eroded Erebus crater. Very large, nontraversable ripples, referred to informally by the project team as purgatoids because of their similarity to Purgatory ripple were 5–10 m across and over a meter high and blocked access to the crater center (Figure 5). *Opportunity* had to traverse west and north to get to the western rim of Erebus to continue its traverse south (Figure 4). No clear craters were observed by *Opportunity* for 455 sols from Viking crater to the edge of Victoria crater annulus (Beagle crater). After reaching Beagle crater (Sol 898), the Victoria crater annulus (~750 m wide or one-crater diameter) offered a smooth, flat, and sandy surface to partially circumnavigate the crater (Figure 4). Around seven smaller craters were imaged by *Opportunity* on the Victoria crater annulus (Tables S1a and S1b).

After exploring the interior of Victoria crater at Duck Bay, the decision was made to traverse around 12 km to the southeast to Endeavour crater [*Squyres et al.*, 2012] (Figure 1), an eroded Noachian 22 km diameter crater with a partially exposed rim with phyllosilicates [*Wray et al.*, 2009]. Inspection of just available HiRISE images [*McEwen et al.*, 2010] showed that huge fields (>3 km wide) of very large, nontraversable ripples surrounded the Victoria crater annulus to the south and east, which prevented planning a straight line path to Endeavour (Figures 1 and 6). These images also delineated the smooth sandy terrain, the large ripple terrain with purgatoids, and beveled outcrop terrain.

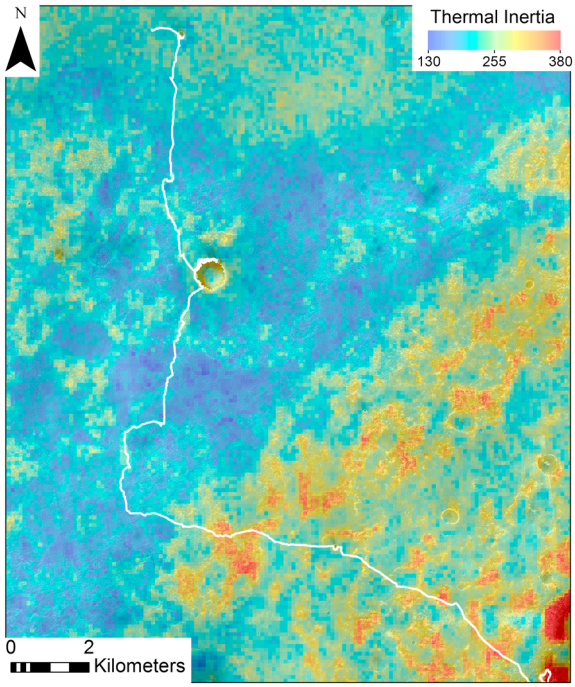

Figure 3. THEMIS thermal inertia overlain on HiRISE mosaic with the rover traverse. Low thermal inertia terrains, recognized prior to landing [*Golombek et al.*, 2003], in the middle part of the traverse correspond to large ripple terrain and fields of purgatoids. Thermal inertia values, in units of J m^{-2} K^{-1} s$^{-1/2}$, from THEMIS infrared data were derived using the method of *Fergason et al.* [2006], including corrections for the time-dependent change in focal plan temperature, the tilt of the spacecraft, and for row- and line-correlated noise [*Christensen et al.*, 2004; *Fergason et al.*, 2006; *Edwards et al.*, 2012]. Nighttime temperatures only were used because the effects of albedo and Sun-heated slopes have mostly dissipated throughout the night, and the thermal contrast due to differences in particle sizes are at a maximum [e.g., *Kieffer et al.*, 1973, 1977; *Jakosky*, 1979; *Palluconi and Kieffer*, 1981]. Map from infrared images I01667003, I11478003, I17306023, and I31594011, acquired during Mars years 26–29 and range in L_s from 5.97° to 199.12°. Area is the same as Figures 1 and 2.

Comparison of these terrains observed in HiRISE with Thermal Emission Imaging System (THEMIS) thermal inertia shows that each has a distinctive signature (Figures 2 and 3). The thermal inertia of the smooth sandy terrain ranges from ~155 to 230 J m^{-2} K^{-1} s$^{-1/2}$ and corresponds to cohesionless fine to very fine sand (particle sizes 63–120 μm) [*Golombek et al.*, 2005]. These surfaces are found in the northern 3 km of the traverse as well as areas between outcrops in the final 8 km of the traverse. The thermal inertia of the large ripple terrain with abundant purgatoids ranges from 140 to 165 J m^{-2} K^{-1} s$^{-1/2}$, corresponding to very fine sand with particle sizes of ~70 μm. The thermal inertia of the large ripples themselves is even lower (~140–145 J m^{-2} K^{-1} s$^{-1/2}$), corresponding to cohesionless silt with particle sizes ~40 μm. These areas correspond to the lowest thermal inertia areas and correlate well with HiRISE-based maps of extensive fields of large ripples (Figure 2). Finally, areas with beveled outcrop have thermal inertias that range from ~160 to 350 J m^{-2} K^{-1} s$^{-1/2}$. Higher thermal inertias correspond to exposed outcrop, and lower thermal inertias correspond to areas with eolian bed forms. Thus, very high thermal inertia material (likely bedrock) is mixing with lower thermal inertia materials within 100 m pixels, resulting in the moderate to relatively higher thermal inertia values observed. Mixed terrains with higher inertia correspond to those with outcrop and smooth sandy surfaces over the final 8 km of the traverse. Mixed terrains with lower thermal inertia are found around Victoria and Nimrod and correspond to areas with large ripples mixed with exposures of outcrop (e.g., Figure 5).

The higher thermal inertia of the smooth sandy terrain compared with the large ripple terrain could be related to the population of large blueberries and dense coarse-grained surface lag that dominate the surface [*Soderblom et al.*, 2004]. The decrease in thermal inertia south of Endurance could be due to the observed decrease in blueberry size [*Weitz et al.*, 2006] or the lower concentration and smaller coarse-grained surface lag. In addition, the increase in number and size of large ripples that are composed of very fine sand [*Sullivan et al.*, 2007] could also contribute. Furthermore, because most sand observed at Meridiani Planum is very fine (~100 μm) [*Soderblom et al.*, 2004; *Herkenhoff et al.*, 2004; *Sullivan et al.*, 2007; *Geissler et al.*, 2010], the large ripples likely are also composed of fine sand. The extremely low inertia of large ripples (implying a 40 μm grain size) is probably partially due to dust. This is consistent with the bright appearance of the large ripple surfaces, attributed to a surface coating of dust. We find support for more dust sequestered from winds among the troughs of the secondary ripples, banked against the west facing flanks of the purgatoids (Figure 5c). Large ripples also have dusty west sides due to prevailing winds but have firm troughs and slightly cohesive east sides [*Sullivan et al.*, 2005, 2007, 2011].

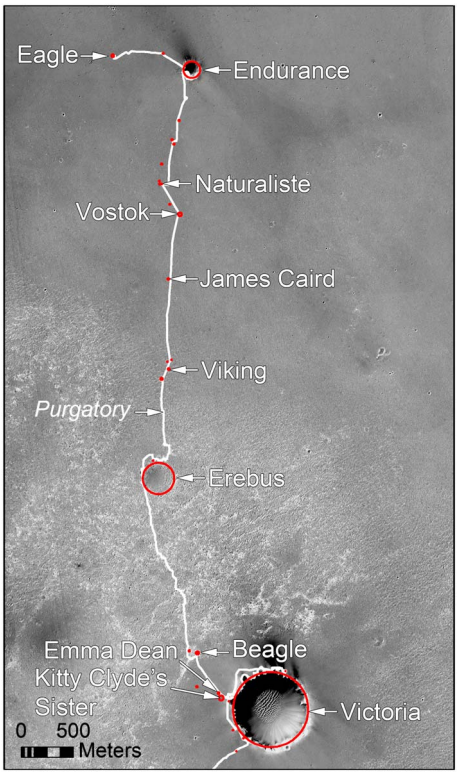

Figure 4. HiRISE image showing the portion of the traverse from the Eagle landing site to Victoria crater. Craters imaged by *Opportunity* along the route are shown in red. Note the smooth sandy surface in the northern part of image (roughly to Viking crater); large ripple terrain with purgatoids between Purgatory ripple and Beagle, and the smooth sandy annulus around Victoria.

To avoid the mapped fields of large, nontraversable ripples, *Opportunity* took a 6 km long west-southwest path to skirt around the largest ripples and then turn to the southeast on smoother mostly sandy and beveled outcrop terrain with smaller and progressively fewer ripples (Figures 1, 3, and 6). After departing the Victoria crater annulus on Sol 1692, *Opportunity* traversed about 1.3 km toward the west-southwest, navigating around large ripples and driving on outcrop or small ripples where possible (Figure 6). Three degraded craters (Ranger, Surveyor, and Half Moon) were imaged along the way. The rover was directed to a crater cluster (Resolution on Sol 1821) that is superposed on and clearly younger than the latest phase of granule ripple migration [*Golombek et al.*, 2010]. After the Resolution crater cluster, the rover continued another 1.3 km south across terrain with moderate size ripples until it came to the northern edge of a large (600 m diameter) very degraded crater called Nimrod. *Opportunity* drove about 1 km to the west and then 2 km to the south imaging seven degraded craters (Gjoa, Falcon, Trinidad, and San Antonio) and was directed to the youngest crater observed (Concepción) (Table 1 and Tables S1a and S1b in the supporting information).

On Sol 2251, *Opportunity* began driving to the east toward Endeavour crater. The next goal was Santa Maria crater, a relatively fresh 93 m diameter crater about 5.4 km to the east-southeast (Figure 6). In that 5.4 km, *Opportunity* imaged ~14 craters with diameters 5–20 m. The first 2 km of this portion of the traverse was on a mostly sandy surface with moderate size granule ripples. The next 1.6 km of the traverse was on a mix of ripples and beveled outcrop, and the final 1.8 km was on a very smooth sandy surface with small ripples. The craters in this section of the traverse are mostly degraded and were targeted as end of drive imaging positions or as middrive imaging stops called "drive by shootings."

After Santa Maria crater (explored during Sols 2450–2554), the rover traversed the last 6.5 km to the southeast in two halves (Figure 7). The first half was about 3.4 km in the east-southeast direction to the Gemini 5 crater; the second half was about 3.1 km to the southeast where it ended at the rim of Endeavour crater at the southern edge of Cape York. *Opportunity* imaged 14 craters during the first half and nine craters during the second half. The terrain traversed during the first half was a remarkably smooth, flat, mostly sandy surface with very small ripples. The ripples were slightly larger during the second half of the traverse and it covered more flat outcrop than the first. During the last ~8.5 km of the traverse, rover drives were not impeded by the terrain and imaging craters required ending the drives near a crater and imaging it or planning a middrive stop.

3. Crater Catalog

Opportunity imaged about 100 craters during the traverse from Eagle to Endeavour crater as shown on Figures 4, 6, and 7. This complete catalog of all craters (informally named after ships of discovery) imaged during the traverse was created by plotting the traverse on HiRISE images, querying the project list of crater names, and searching the project database of surface activities. For this paper, we restrict our search to craters on the sandy surface underlain by the Burns formation (Eagle to Endeavour) as crater retention appears to be different on the older Noachian rim terrains of Endeavour crater. We include craters that *Opportunity* imaged closely enough to show the morphology of their interior, rim, and ejecta. The crater floor

Table 1. Catalog of Craters Imaged by *Opportunity* on Meridiani Planum Described in the Text (See Tables S1a and S1b in the Supporting Information for Complete Catalog)

Crater	Sol Imaged	Diameter (m)	Depth (m)	Morphology	Morphologic Class	Estimated Age (Ma)	Degradation Rate (m/Myr or m/yr)
Eagle[a,b]	1–60	22	2	Sandy interior, limited exposed outcrop mostly planed off along portion of interior wall, ripples cover slightly raised rim	5	4–10	0.34
Emma Dean	931	16	1	Mostly sandy crater with elevated rim, scattered outcrop mostly planed off, ripples along rim	4	2–4	0.73
Kitty Clyde's Sister	943	46	<1	Rimless[c] shallow depression, rim defined by few planed off blocks, ripples pervade interior of crater	6	20	0.55
Kaikos[d]	1950	6	~1	Blocky uplifted rim and interior wall, blocky ejecta, some blocks planed off, sandy interior	2	0.2–0.6	0.5
Nerius[d]	2011	9	~2	Blocky uplifted rim and interior wall, blocky ejecta, some blocks planed off, sandy interior	2	0.2–0.6	0
Nautilus[d]	2011	6	~1	Blocky uplifted rim and interior wall, blocky ejecta, some blocks planed off, sandy interior, ripples merge with rim	2	0.2–0.6	0.5
Concepción[d]	2139–2178	10	1	Very fresh-rayed crater, ejecta blocks on top of ripples, some blocks etched and sand deposited between ejecta blocks, sandy interior	1	~0.1	10
Voskhod	2441	15	0.6	Sandy depression with slightly elevated rim, few planed off blocks in small portion of rim, ripples form part of rim, no ejecta	5	4–10	0.34
Santa Maria	2453	93	16	Elevated rim, sandy interior with dunes, mostly planed off ejecta blocks in backwasted rim and adjacent blocks in rays are planed off within one-crater diameter, secondaries outside one-crater diameter, ripples overlie rays	3	0.6–2	2.6

[a]Included in *Golombek et al.* [2006a].
[b]Included in *Grant et al.* [2006a, 2008].
[c]Use of the term, rimless, is to indicate that no positive relief rim is present.
[d]Included in *Golombek et al.* [2010].

could be seen in almost all cases and so depth and diameter were measured using stereo Navcam and Pancam images using the Maestro mission planning and data display software [*Parker et al.*, 2010, 2012; *Powell et al.*, 2010]. Crater diameters were generally less than 50 m and were imaged from typically within about 10 m of the rover (Tables 1 and S1a). Stereo ranging errors for Navcam images are around 1% of the distance [*Maki et al.*, 2003], implying ideal uncertainties that vary from about 1 cm for measurements at a distance of 1 m to 0.1 m for measurements at distances of 10 m (or about 1%). We also measured crater diameters in HiRISE images, for cases where rims could be discerned (generally craters larger than about 2 m diameter). These diameter measurements generally agreed to better than 10% with those derived from the Navcam images. Because most craters are less than 10 m diameter and shallow, accurate depths could not be obtained from HiRISE digital elevation models.

The catalog also includes the HiRISE image of the crater, along with the traverse path and rover location and sol where surface images were acquired as well as the surface images of the crater. For each crater, the morphometry (depth and diameter) and morphology of the interior, rim, and ejecta were included. In most cases, small craters were targeted in planning the path (section 2) and it was common to deviate up to 100 m to get close enough to image the craters either at the end of a drive or during middrive imaging. In general, fresher craters stood out more in the HiRISE images and were easier to distinguish in surface images and so were targeted for imaging more often than very degraded or inverted craters that can be seen in MOC or HiRISE images (e.g., section 5.1).

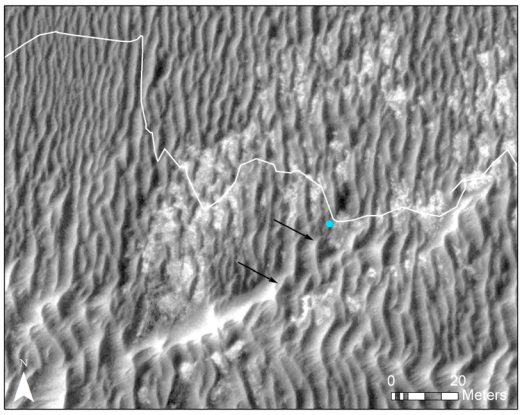

a)

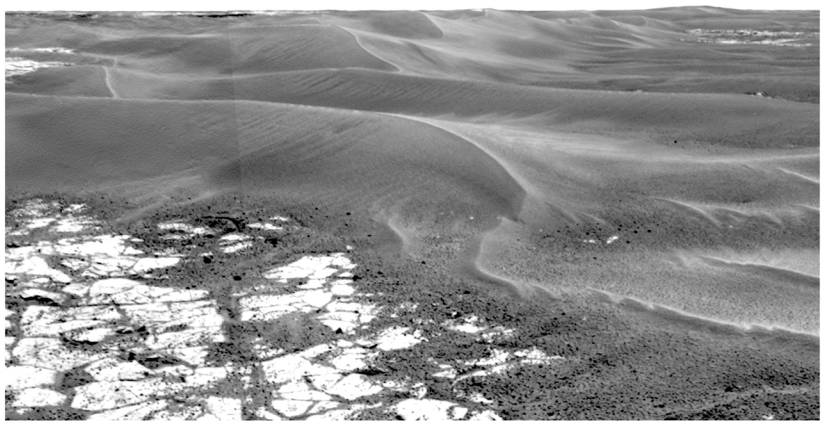

b)

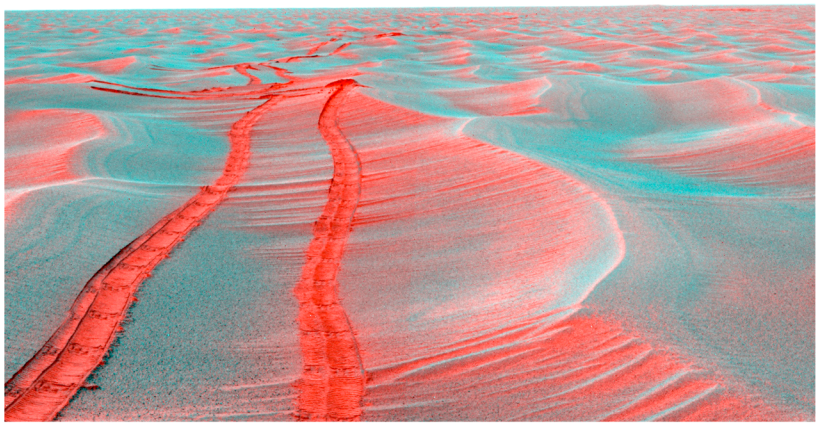

c)

Figure 5. (a) HiRISE and (b) rover view of a wall of large, nontraversable ripples along the northern edge of Erebus crater that blocked access to the crater interior. These ripples forced a traverse west and then north to get to the western rim of the crater in order to continue south. Blue dot shows the location of the rover on Sol 615 when Navcam image (Figure 5b) was acquired, looking southwest at large ripples over 1 m high with steep flanks (examples shown by arrows). (c) Pancam false color mosaic acquired on Sol 512 with red filter (753 μm) mapped to red, and blue filter (432 μm) mapped to green and blue. This view looks north and shows air fall dust (bright red) protected in the troughs of the secondary ripples that are mostly banked against the west facing flanks of the larger primary ripples. Rover tracks also appear red because dust is an important component of the near-subsurface regolith all along *Opportunity*'s traverse and rover wheel tracks compressed the less dusty surface lag into this material (a phenomenon also observed in the airbag bounce marks). The air fall dust could be responsible for the low thermal inertia in regions where the larger ripples (and their dust-protecting secondary ripples) are common.

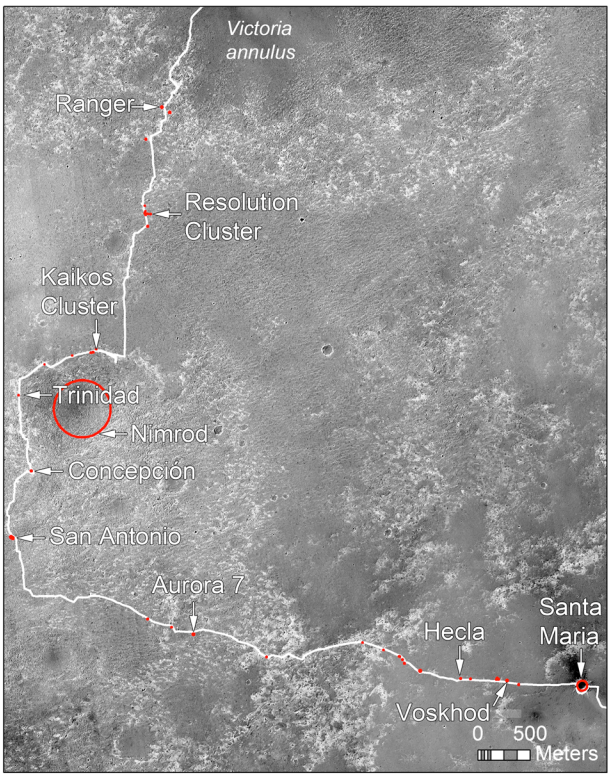

Figure 6. HiRISE image of the portion of *Opportunity*'s traverse from the Victoria annulus to Santa Maria crater. Notice large ripple terrain to the south of the Victoria annulus and south of the Kaikos cluster and Nimrod crater that forced the longer traverse to the south-southwest. Outcrop dominates the traverse route between Aurora and west of Hecla and smooth sandy terrain beyond Hecla to Santa Maria. Craters imaged by *Opportunity* are shown in red.

The complete catalog includes 100 craters, resulting from around 70 falls (some were crater clusters). Each crater and/or cluster has a unique name. Table 1 includes a portion of the catalog (see Tables S1a and S1b for the complete catalog that includes crater name, sol imaged, diameter, depth, morphology, morphologic class, age, and degradation rate). None of the craters had characteristics (e.g., in linear rays or chains) that would indicate that they are secondaries, formed by the impact of ejecta from a primary crater elsewhere. Almost all of the craters in the catalog are less than 50 m diameter, with only Santa Maria (93 m), Endurance (150 m), and Victoria (750 m) larger (included because the rover examined them in detail). The vast majority of the craters observed are less than 20 m diameter (91% of the sample). Of these, 68% of the sample is $<$10 m diameter and the mode is 6–10 m in diameter (40% of the sample). The smallest crater in the catalog is 1 m; about 90% of the craters are $>$3 m diameter.

The number of craters observed by the rover in different portions of the traverse can be related to the surface terrains and the ability of the rover team to identify craters in these terrains. There are 16 craters from Eagle to just north of Erebus in the smooth sandy surface with small ripples (~5 craters/km of traverse). In contrast no craters were identified in the area north of Erebus to Beagle crater near the Victoria annulus in which large ripples are present. From Victoria to Santa Maria there are about 22 craters and from Santa Maria to Endeavour around 24 craters. These numbers correspond to around five craters per kilometer of traverse in smooth terrain with small ripples and around one crater per kilometer of traverse in terrain with large ripples. This suggests that areas with large ripples (and more abundant sand) degrade small craters faster than smoother sandy surfaces with small ripples. Small craters were also harder to identify in orbital images and from the surface in large ripple terrain. We see the same relations in craters observed in HiRISE images (section 5.1).

4. Crater Morphology and Degradational State

Small craters observed by *Opportunity* are in a variety of degradational states. The freshest craters have sharp, elevated rims and blocky ejecta (when impacted into sandstones). Crater interiors are bowl (or flat-bottomed cone) shaped with steep inner walls that are also blocky when the impact occurs into Burns formation. Ejecta and rims are superposed on the granule ripples. With time, the ejecta is worn down and planed off, the rim is eroded down and back wasted, and the interior is filled with sand. The most eroded craters are rimless depressions sometimes with planed off sandstones that form a ring with no ejecta. Ripples sometimes form on the rim and cross the crater. *Grant et al*. [2006a]; *Golombek et al*. [2006a] and *Golombek* [2012] document this degradational sequence for Meridiani craters, and from this work we recognize six degradational states (class 1, freshest, to class 6, most degraded) based on the crater morphology and the state of their rims, ejecta, interior and inner wall, and their interaction with ripples [*Golombek et al*., 2010] (Table 2).

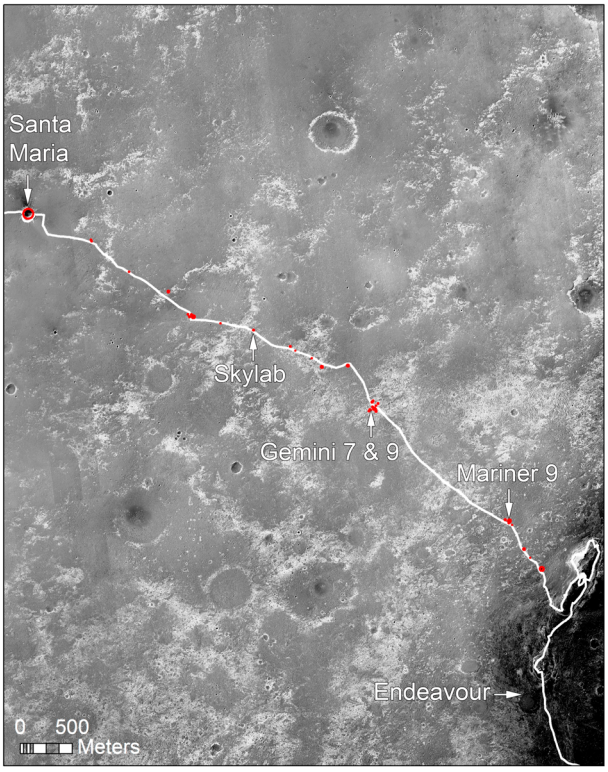

Figure 7. HiRISE image of the portion of the traverse between Santa Maria and Endeavour craters that is dominated by smooth sandy terrain with outcrop exposure. Craters imaged along the traverse are shown in red. Gemini 5 crater is the next crater northwest of Gemini 7 and 9 craters.

4.1. Class 1 Craters

Class 1 craters imaged by *Opportunity* have elevated rims, bowl shapes, blocky ejecta, blocky inner walls and rims (if impacted in sandstone), sharp rims (if they formed in sand), and they are superposed on the granule ripples [*Golombek et al.*, 2010]. Class 1 craters that have been visited by *Opportunity* include the Resolution crater cluster and Concepción crater. Concepción crater has a blocky rim and blocky ejecta arranged in rays that overlie the granule ripple surface. Outside of dark sand on the crater floor and dark sand among some ejecta, the crater is unmodified by eolian bed forms (Figures 8 and 9). In HiRISE images, class 1 craters can be distinguished by ejecta and rays that overlay the granule ripples (Figure 8), crater rims that truncate the granule ripples (Figures 8 and 9), and rims that are unmodified by large ripples [*Golombek et al.*, 2010]. A little over 10% of the catalog is composed of class 1 craters, although all but one are associated with the Resolution cluster of 10 craters, which represents one fall.

4.2. Class 2 Craters

Class 2 craters imaged by *Opportunity* have elevated rims, partially planed off blocky ejecta and inner walls, sandy interiors, and ripples that merge with their rims. Kaikos, Nerius, and Nautilus (Figures 10 and 11) are examples of this morphologic class (as is Skylab). They have blocky rims and inner walls, but some of the ejecta is planed off. The rims are rounded and the floor is sandy. The HiRISE images show that ripples merge with the crater rims, indicating that the ripples were active after the craters formed. About 5% of craters in the catalog are class 2 craters.

Table 2. Morphologic Classification of Craters

Classification	Age	Typical Morphology
Class 1	<50–200 ka	Elevated sharp rim, bowl shape, blocky ejecta on ripples, rays superposed on ripples
Class 2	~200–600 ka	Elevated rounded rim, sandy interior, partially eroded blocky ejecta and interior wall, ripples merge with rim
Class 3	~0.6–2 Ma	Elevated but degraded and mostly smooth rim, blocky interior wall, sandy floor sometimes with bed forms, ejecta mostly planned off, ripples merge with rim
Class 4	~2–4 Ma	Slightly elevated rim, ejecta blocks completely planned off, shallow sandy interiors, ripples merge with and modify rim
Class 5	~4–10 Ma	Rimless[a], shallow sandy interior, no ejecta, ripples modify rim
Class 6	~10–20 Ma	Rimless very shallow sandy depression, ripples form rim and cross the interior, planed off blocks may form rim, no ejecta

[a]Use of the term, rimless, is to indicate that no positive relief rim is present.

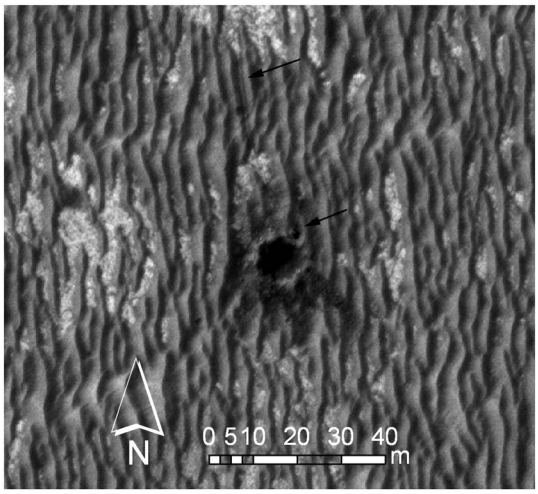

Figure 8. HiRISE image of Concepción crater (class 1) showing blocky rim and ejecta and dark rays, the best defined extending to the southeast from the crater. The crater clearly truncates and the rays are superposed on the ripples. *Opportunity* is perched on the northeast rim (note the shadow cast to the southeast; lower arrow) on Sol 2153 and the rover tracks are visible from the north (upper arrow). HiRISE image ESP_016644_1780.

4.3. Class 3 Craters

Class 3 craters imaged by *Opportunity* have elevated rounded rims, mostly planed off blocky ejecta, blocky inner walls, and shallow sandy floors commonly with bed forms and ripples that merge with their rims. Craters in this morphologic state include Fram, Viking, Vega, Beagle, Granada, Intrepid, Santa Maria, Gumdrop, and Mariner 10.

Santa Maria crater is a 93 m diameter, class 3 crater with key relations that the rover was directed to and explored from sol 2450–2554. In HiRISE images, the crater has a sharp, irregular rim with eolian bed forms on its floor (Figure 12). Light-toned rays extend to a distance of about one-crater diameter, but the ejecta in the rays appear planed off. Secondary craters begin beyond the rays and extend several crater diameters. *Opportunity* confirmed most of these observations. Although the crater has an elevated rim, the surroundings are smooth and almost all of the ejecta have been planed off (Figure 13). Large eolian bed forms are found inside the crater, and the inner wall of the uppermost crater rim shows ejecta blocks that have been planed off and exposed by backwasting (Figure 14). This relation is also seen at Endurance and Victoria craters [*Grant et al*., 2006a, 2008] and demonstrates that the ejecta is easily planed off by the saltating sand. In addition, because most of the one-crater diameter annulus is sand covered at the surface, the sand both planes off the surrounding ejecta and then eventually covers it. The ejecta observed in the inner wall of the crater indicate that only a portion of the ejecta is planed off before it is covered with sand. Victoria crater also has a distinctive annulus that is sand covered but has ejecta preserved in its inner rim [*Grant et al*., 2008]. These observations indicate that discontinuous layers of planed off ejecta could be hidden beneath the sandy surface of Meridiani Planum. Images of Maniwa Ray show that ejecta blocks have been planed off parallel to the surface and ripples overlay the planed off blocks, indicating that the ripples are younger than the crater (Figure 15). About 8% of craters in the catalog are composed of class 3 craters.

4.4. Class 4 Craters

Class 4 craters have slightly elevated rims, shallow sandy interiors, completely planed off ejecta blocks, and ripples that modify their rims. Craters in this morphologic state include: Endurance, Potato Furrow,

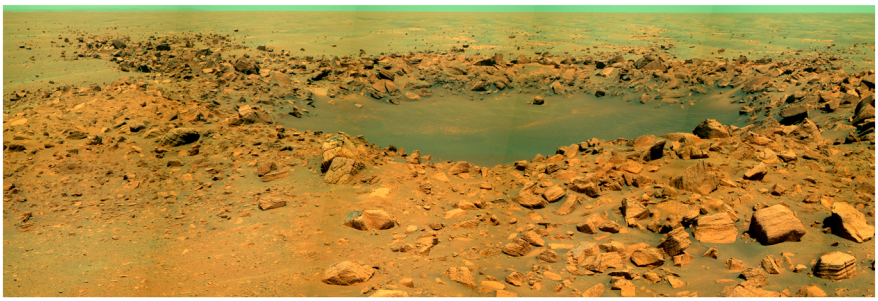

Figure 9. Pancam false color mosaic looking toward the south of class 1 Concepción crater acquired on Sols 2139–2141 when *Opportunity* was about 5 m from the north rim. Ejecta of sulfate bedrock is scattered across the surface and in blocky rays and are clearly younger than the ripples. The dark rays observed in the HiRISE image are produced by the shadows and shading from the blocky ejecta in the low Sun image (Sun angle is 36°). The interior of the crater is covered in dark sand, which also fills in among the ejecta blocks in the lower right of the mosaic.

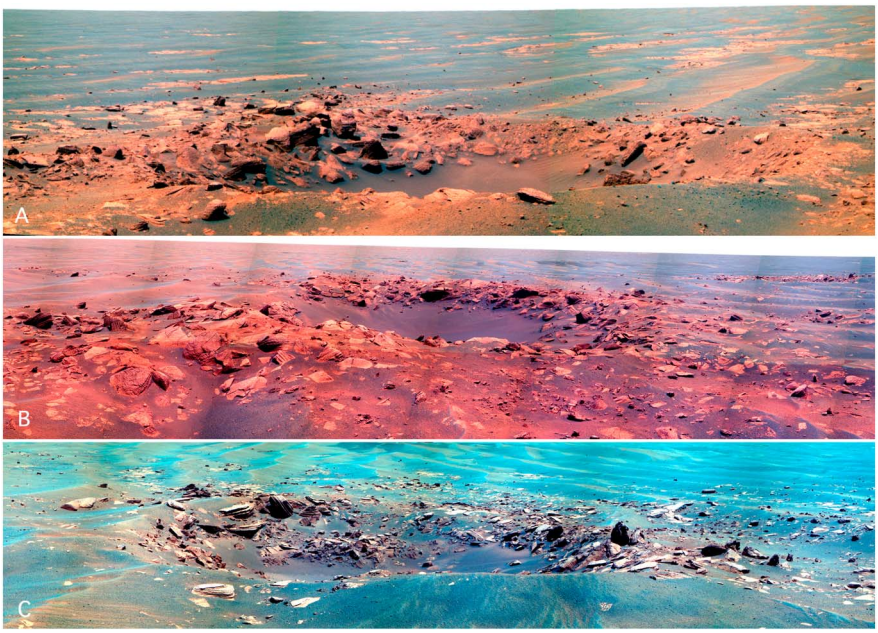

Figure 10. Pancam color (true and false) image mosaics of (a) Kaikos, (b) Nereus, and (c) Nautilus craters, the three largest craters in the Kaikos cluster. The craters are relatively fresh (class 2), but the rims appear somewhat smooth and rounded, some ejecta blocks appear partially planed off parallel to the surface, and ripples merge with the crater rims (see especially the near rim of Nautilus), indicating that the craters have been partially modified by the ripples.

Naturaliste, Géographe, Investigator, Nina, Voyager, Emma Dean, Sputnik, Chatum, Scotia, Ranger, Surveyor, Half Moon, Pembroke, Gjoa, Falcon, Trinidad, San Antonio, Paramore, Yankee Clipper, Antarctic, Sigma 7, Freedom 7, Friendship 7, Molly Brown, Gemini 5, and Mariner 9. Emma Dean crater (Figure 16) is a shallow sandy crater with sandstone blocks almost completely planed off. Most ejecta blocks are also planed off, but little of the ejecta remain. Ripples merge with and modify the slightly elevated crater rim. In the HiRISE image a few vestigial rays are present and ripples merge with the rim (Figure 17). About 37% of craters in the catalog are composed of class 4 craters.

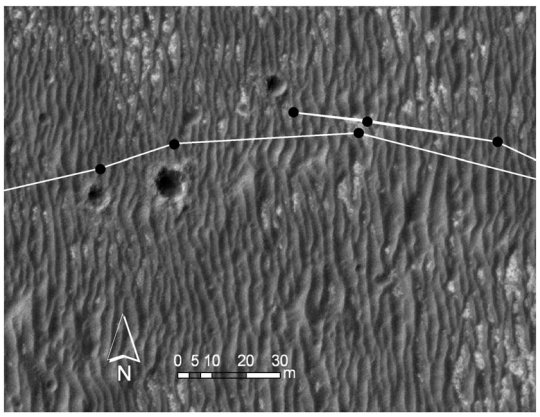

Figure 11. HiRISE image ESP_012820_1780 of the Kaikos crater cluster first visited by *Opportunity* on Sol 1950 in southern Meridiani Planum. Kaikos crater (6 m in diameter) is the farthest east and was imaged on Sol 1950. After backtracking to investigate Block Island (a large iron meteorite to the east), Nereus, the largest crater (9 m in diameter), was imaged on Sol 2009. Nautilus crater (6 m in diameter) is to the west and was imaged on Sol 2011 (black dots are rover image locations). The rims of these craters appear somewhat blocky in this image, but on close inspection several ripples appear to merge with the crater rims, indicating that these craters are partially modified by the ripples, suggesting that they impacted before the latest phase of ripple migration and are thus class 2 craters. Smaller craters of this cluster are to the southeast [*Golombek et al.*, 2010].

4.5. Class 5 Craters

Class 5 craters are rimless (elevated rims have been eroded away), mostly sandy depressions, with no ejecta and ripples that merge with and follow the edge of the crater. Class 5 craters imaged by *Opportunity* include: Eagle, Argo, Alvin, Jason, Trieste, Gauss, Jaims Caird, Victoria, Kainan Maru, Kitty Hawk, Lightening, Gabriel, Virginia, Southern Cross, Golden Hind, Hecla, Fury, Vanguard, Voskhod, Salyut, Casper, Joliba, Faith 7, Gemini 4, Chikyu, and Spider. Voskhod crater is an example of a class 5 crater (Figures 18 and 19). It is a shallow sandy depression, with no ejecta. Blocks in a small portion of the inner wall are planed off (Figure 19). Ripples merge with and form the rim of the crater. In the HiRISE image the crater shows up as

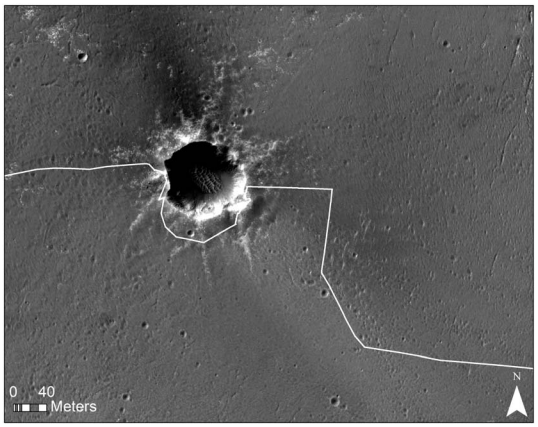

Figure 12. HiRISE image with rover traverse (Sols 2450–2554 from west to east) near Santa Maria crater, a class 3 crater (north is up). Note the serrated crater rim, eolian bed forms on floor, light-toned rays with little relief that extend about one-crater diameter away, and secondary craters beyond (e.g., crossed by rover to the southeast).

a circular depression with a bright rim and dark interior (Figure 18). About 30% of craters in the catalog are composed of class 5 craters.

4.6. Class 6 Craters

Class 6 craters are rimless, very shallow, mostly sandy depressions, with no ejecta. If blocks are present, they are planed off and sometimes form a circle where the rim once was. Ripples cross the crater and/or are where the rim once was. Very degraded craters imaged by *Opportunity* include: Vostock, Snoopy, Kitty Clyde's Sister, Aurora 7, Aquarius, Apollo 7, Gemini 7, Gemini 9, and Pathfinder. Ripples cross Kitty Clyde's Sister, and rim blocks are completely planed off (Figures 17 and 20). There is no ejecta, and the 46 m diameter crater is $<$1 m deep. About 10% of craters in the catalog are composed of class 6 craters. The largest craters in the catalog (all but one crater larger than 20 m diameter, excluding Endurance, Victoria, and Santa Maria) are class 6 craters.

5. Crater Ages

To estimate the ages of craters in different degradational states, we first establish the crater retention age of all small craters on Meridiani Planum near the traverse. Next we use the age of the latest phase of ripple migration around 50–200 ka to distinguish craters that are younger and older. Finally, we use the craters in the catalog to construct size-frequency distributions and inferred ages from crater age isochrons.

5.1. HiRISE Crater Retention Age

To estimate the ages of craters in different degradational states, we first establish the crater retention age of all small craters near the traverse. Previous crater counts of Meridiani Planum display a surface with two ages. Craters larger than about 2 km diameter are highly degraded with light-toned rims that define a latest Noachian age [*Hynek et al.*, 2002; *Lane et al.*, 2003; *Arvidson et al.*, 2006]. These craters correspond to the age of the Burns formation sulfate sandstone outcrop investigated by the *Opportunity* rover. *Lane et al.* [2003] found that craters between about 10 m and 100 m diameter measured across the general region in a number of MOC images fall on an isochron of ~10 Ma using the *Hartmann and Neukum* [2001] chronology function and the *Ivanov* [2001] crater production curve. These craters fall on the ~20 Ma isochron using the updated *Hartmann* [2005] functions. Here we refine the crater retention age along the rover traverse by crater counting a 500 m swath on either side of the rover traverse in HiRISE images (Figure 2). The count includes all craters (primaries and randomly distributed secondaries) $>$5 m in diameter and does not differentiate between degradational states, incorporating the freshest craters that superpose bed forms as well as planed off and inverted crater forms that are more difficult to identify in rover images. Three terrain types were also mapped within the swath to determine how crater retention varies (Figure 2). Each terrain type has distinct albedo, textural, and thermal characteristics (Figure 3) that correspond with differences in impact crater

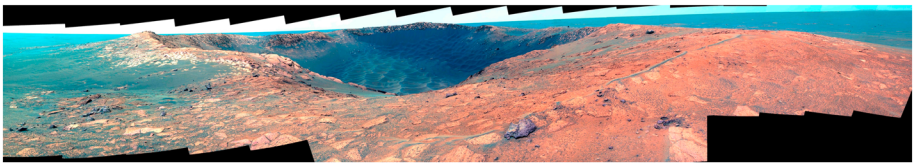

Figure 13. Pancam false color mosaic of Santa Maria crater (class 3) acquired on Sol 2512 when *Opportunity* was on the southeast rim. This crater still has an elevated rim, but almost all of the ejecta has been planed off and covered by sand away from the rim. Note the small ripple along the rim to the right.

density. These terrains include the exposed light-toned, fractured bedrock of the Burns Formation, the large ripple terrain, which includes purgatoids and small exposures of bedrock, and smoother sandy surfaces with smaller ripples.

The cumulative frequency plot (Figure 21) illustrates the distribution for all craters within the swath as well as each terrain type as measured in HiRISE images. Model age fits were constructed using the *Hartmann* [2005] chronology and production functions in craterstats2 [*Michael and Neukum*, 2010]. All model age uncertainties quoted here are from counting statistics alone and do not include systematic uncertainties such as calibration of the crater chronology functions and other factors. Furthermore, the plots report up to three significant figures, which is the direct output of the craterstats program. Within the text we provide these ages but summarize our data using one significant digit (Tables 2, S1a, and S1b). The data for each terrain type demonstrate a single kink that separates the larger diameter, more ancient population from the younger, smaller diameter population ($D < 35$ m). The slope of the distribution crosses multiple isochrons for craters >35 m diameter, suggesting significant erosion of this population since the original surface formed. No crater larger than 750 m (Victoria crater) was present within the count area. For each cumulative frequency plot, a resurfacing correction was applied in craterstats to the post-resurfacing crater population [*Michael and Neukum*, 2010; *Platz et al*., 2013].

All craters <35 m in diameter that are along the traverse parallel the 25 ± 0.4 Ma isochron, which is interpreted as a crater retention age for the region. This model age does not however differentiate between crater statistics from the different terrains that exhibit varying degrees of crater exposure and preservation. Bedrock exposures, for example, show the highest crater density (and the largest number of highly degraded craters) as well as local clustering that is due to differential burial from bed forms. Within the <35 m diameter range the crater retention age of the bedrock only region, excluding bed forms where possible, is 71 ± 2 Ma. The crater density and model age for the bedrock region of the traverse are significantly higher compared to all other terrains due to the inclusion of extremely degraded crater forms. These craters represent a degradational class (a seventh, more degraded class) that was not characterized by the rover (due to difficulty in ground-based detection) and are only obvious in HiRISE, represented by quasi-circular ghosts or inverted crater forms that are sites of preferential ripple accumulation. These degraded landforms are also visible in HiRISE on the other terrain types but not in such high density. This suggests that the bed forms at these locations either cover the degraded craters or erosion completely removed them.

The majority of the rover traverse crosses surfaces covered by large ripples and smooth sandy surfaces with small ripples. These HiRISE crater retention data from these terrains are therefore more representative of our sample set from the six degradational classes described in section 4. Both of these terrain types exhibit a similar crater retention age of roughly ~20 Ma (18 ± 0.6 Ma for the large ripple terrain and 23 ± 0.6 Ma for the smooth terrain, respectively). The slightly younger age and shallower slope of the crater distribution in the large ripple terrain relative to the smooth terrain, which also exhibits a near-continuous cover of sand, may suggest that smaller craters are being preferentially eroded here. The mean crater density varies from 65 craters/km^2 (>5 m) on terrains with large ripples to 127 craters/km^2 on the smoother terrain. This is also consistent with fewer craters observed by *Opportunity* in the large ripple terrain (section 2). We conclude that a crater retention age of ~20 Ma is most representative of the six classes of craters that were characterized in situ by the rover; the crater catalog does not include the seventh, most degraded class of crater forms that are exposed preferentially on the bedrock terrain but not characterized by the rover.

5.2. Craters Younger and Older Than Granule Ripple Migration

The youngest craters (class 1) observed by *Opportunity* are the Resolution crater cluster and Concepción craters, which are clearly superposed on the granule ripples and thus younger than the latest phase of ripple migration [*Golombek et al*., 2010]. Two larger, fresh-rayed craters in Meridiani Planum that were imaged by HiRISE bracket ripple migration; secondaries from 2.2 km Ada crater are clearly superposed on the ripples, and secondaries from an unnamed 0.84 km diameter crater have been modified and overprinted by the ripples. Three largely independent methods were used to estimate the age of these craters [*Golombek et al*., 2010]: (1) measuring only the freshest unmodified craters in a portion of a HiRISE image around Resolution crater, (2) estimating the age of Ada and the unnamed 0.84 km diameter crater from younger craters superposed on their continuous ejecta blankets, and (3) estimating the expected recurrence intervals of similar diameter fresh-rayed craters in the equatorial region of Mars compared with the two Meridiani craters. All three

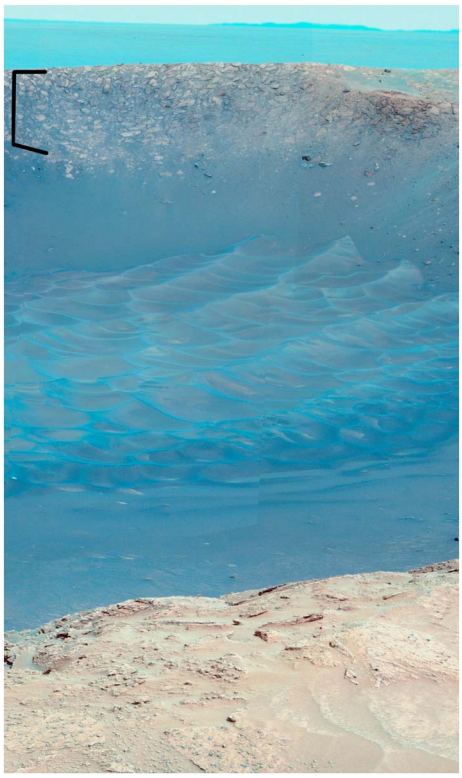

Figure 14. Pancam false color image acquired on Sol 2453 of Santa Maria crater (class 3) showing eolian bed forms on the floor, and ejecta on the inner wall has been planed off (denoted by bracket) by back-wasting of the rim.

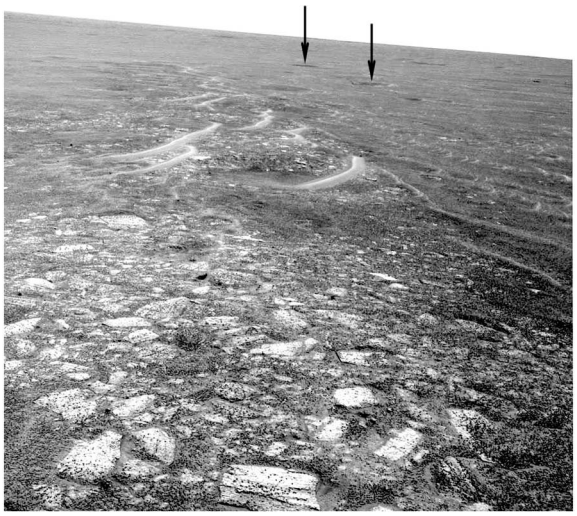

Figure 15. Navcam image of Maniwa Ray showing ejecta blocks have been planed off parallel to the surface and ripples overlay the planed off blocks. Navcam of the ray acquired on Sol 2474 when *Opportunity* was south of Santa Maria crater (class 3 crater) looking away from the crater to the south. Note the small secondary craters in the distance (two denoted by arrows).

methods constrain the latest phase of granule ripple migration to have occurred between ~50 and ~200 ka [*Golombek et al*., 2010].

5.3. *Opportunity* Crater Count Ages

The ages of craters in six different degradational states were determined using crater counts and comparison to crater age isochrons using both incremental and cumulative plots. The length of the *Opportunity* traverse from Eagle to Endeavour in which the craters in the catalog were imaged is ~33.5 km long. To image craters from a nearby position the rover deviated from the selected path (section 2) by up to ~100 m. As a result, the crater catalog can be considered a sample of visible craters within a swath that is 33.5 km long by 0.2 km wide. This allows us to plot the size-frequency distribution of craters in different degradational states in the catalog to derive a crater age for each (Figure 22). Incremental plots (Figure 23) were constructed first for each set of classes (e.g., classes 1 to 6 and 1 to 5) to determine the model age at each crater diameter bin (see Table S2) and to define cutoff diameters for crater populations that either fall on a distinct isochron or cross multiple isochrons. This method informed our application of model age fits and resurfacing corrections to a specific range of crater diameters on cumulative frequency histograms (Figure 22).

The rover only imaged a portion (~100) of all the craters within the 200 m wide swath. The craters >5 m diameter counted in HiRISE number 842 within ±100 m of the rover path, indicating that the rover imaged only about 12% of the craters present. However, comparison of the craters that the rover imaged with those seen in HiRISE shows that the rover imaged about 90% of the class 1–5 craters, which show up prominently in the HiRISE image. The craters that were not imaged by the rover include craters that are even more degraded than class 6, including quasi-circular ghost and inverted crater forms. As a result, the missed craters will have the greatest affect on the derived model age for the total (classes 1–6) or oldest population of craters. This is represented by a deviation of the size-frequency distribution of craters to slopes that are lower than the established isochrons. Finally, a number of the craters in the catalog are doublets or clusters or parts of clusters. For these we calculate an effective crater diameter using $D_{\mathrm{eff}} = (\Sigma D_i^3)^{1/3}$ [*Ivanov et al*., 2008, 2009; *Daubar et al*., 2013]; D_{eff} for the Resolution and Kaikos clusters are taken from *Golombek et al*. [2010]. None of the

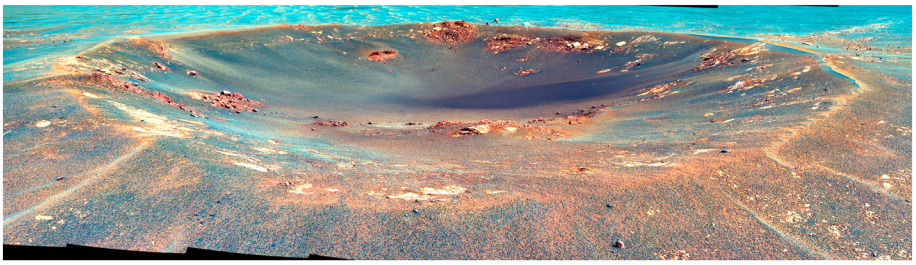

Figure 16. Pancam false color mosaic of class 4, Emma Dean crater, looking south and acquired on Sols 931–938. Note the sandy floor and ripples that merge with the rim and planed off ejecta.

craters in the catalog are obvious secondaries (e.g., in linear rays or chains). However, even if some of the craters are secondaries, the *Hartmann* [2005] isochrons are supposed to include far-field secondaries and so can be used to derive a model age.

For all craters in the rover catalog (classes 1–6), the derived model ages (Table S2 and Figures 22 and 23) range from ~1 Ma for ~5 m craters to ~140 Ma for >100 m craters. However, over the diameter range of ~26 m to 52 m (incremental root 2 bins), including eight craters, the model ages fall between ~10 and 20 Ma, which is consistent with our HiRISE model ages for the smooth and large ripple terrains that dominate the traverse. Fitting the 26 m to 52 m diameter range on the cumulative plot and applying a resurfacing correction [*Michael and Neukum*, 2010; *Platz et al*., 2013] results in a ~15 ± 5 Ma model age (Figure 22) for class 6 craters. The generally lower slope of the distribution and the flattening at <26 m crater diameters suggests that meter-sized craters are being destroyed more rapidly than larger craters. However, by comparison to the rover-derived counts, sampling of ghost and inverted craters in the 5 m to 26 m diameter range with HiRISE bolsters the crater distribution over this range (compare Figure 22 with Figure 23). The roll off in the rover catalog is consistent with the rover not visiting these nearly flat or inverted landforms during the traverse. Larger than 52 m diameter, the distribution of the three largest craters (Santa Maria, Endurance, and Victoria) flattens out considerably. This flattening is consistent with our HiRISE counts (Figure 21) where the slope of the distribution decreases at craters >35 m in diameter and the counts of *Lane et al*. [2003], where the distribution connects to Noachian ages for craters larger than ~1 km. Whereas the incremental and cumulative frequency distributions illustrate that the data for classes 1–6 follow the isochrons reasonably well over the 26 m to 52 m diameter range, the overall slope of the crater size-frequency distribution is lower than the model isochrons, crossing from 10 to 20 Ma on the incremental plot and from 10 to 50 Ma on the cumulative plot. This is also consistent with some degraded craters, even in this diameter range, not being imaged by the rover, including the most degraded class of craters that provides a ~70 Ma crater retention age on the cumulative frequency histogram for bedrock terrains in HiRISE.

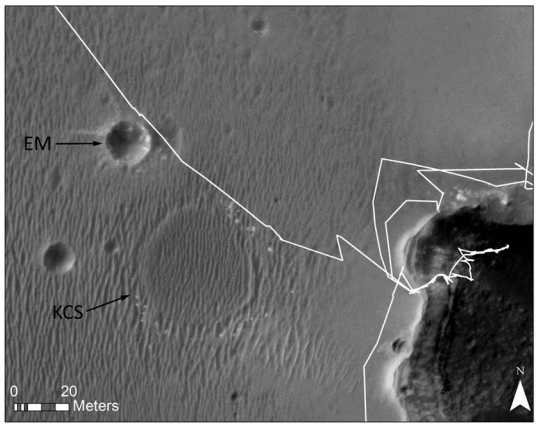

Figure 17. HiRISE image of class 4, Emma Dean crater (EM) and rover traverse. Other craters are the northwest rim of Victoria (southeast) and Duck Bay (where the rover entered the crater) and Kitty Clyde's Sister (KCS), a class 6 crater (central), imaged from the northeast. Sputnik crater is the small, 7 m diameter crater adjacent to Victoria.

For class 1 to 5 craters, the incremental data provide a somewhat consistent model age of 4 to 10 Ma from 22 craters over the diameter range of 13 m to 26 m (see Table S2). Below that range, the incremental plot shows a rapid age roll off, consistent with the preferential destruction of meter-sized craters. Above this range, only a single crater is available that indicates a ~140 Ma model age. A model fit and resurfacing correction was applied to the 13 m to 26 m diameter range on a cumulative frequency histogram, providing a 6.9 ± 2 Ma model age (Figure 22). For class 1 to 4

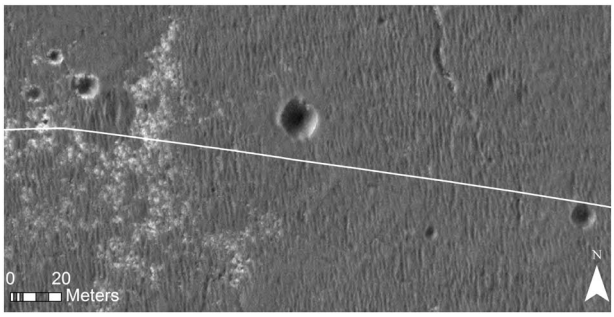

Figure 18. HiRISE image of class 5, Voskhod crater (center) imaged at a stop on Sol 2441 just to the south along the rover traverse. Vanguard craters are to the west and Salyut crater is to the east.

craters, the incremental data provide a range of ages from 2 Ma to 4 Ma for diameters of 9 m to 19 m, which includes 20 craters (Table S2 and Figure 23). The cumulative size-frequency distribution illustrates that this same diameter range crosses the 2 to 4 Ma isochrons, thereby providing a model age (with resurfacing correction) of 2.7 ± 0.6 Ma. At diameters <9 m, the distribution of class 1–4 craters rolls off and becomes shallower than the isochrons (Figures 22 and 23). For class 1 to 3 craters in the catalog, the incremental data provide a tight model age range from 0.8 to 2 Ma over the 9 m to 26 m diameter range (Table S2), indicating that *Opportunity* sampled the majority of the craters from these three classes. Only three crater data points are available both above and below this diameter range. The model age fit with a resurfacing correction was applied to 10 impact craters in this diameter range on the cumulative frequency plot (Figure 22). The fit here indicates a 0.9 ± 0.3 Ma model age. For class 1 and 2 craters, the incremental data include only four impact craters that range in size from 9 to 13 m. All four craters follow the 200 ka to 600 ka isochrons in both the incremental and cumulative plots. There is no roll off at smaller diameters or flattening at larger diameters, and the slope of the distribution matches the isochrons, indicating that the rover sampled the entire (albeit limited) population at this diameter range for these two fresh classes. A model age fit and resurfacing correction provides a 400 ± 200 ka model age. Finally, the distribution of class 1 craters in the catalog (the Resolution cluster and Concepción) yields a derived age of 230 ± 200 ka, which is consistent with our earlier derivation of an age less than ~50–200 ka for craters younger than the latest phase of ripple migration [*Golombek et al.*, 2010].

5.4. Ages of Craters in Different Morphologic/Degradational States

Using all of the ages and constraints discussed above, we can ascribe ages to the craters in each morphologic class (Tables 2 and S1). Class 1 craters are younger than the latest phase of granule ripple migration and are therefore <50–200 ka. Class 2 craters are older than the latest phase of granule ripple migration and are therefore >50–200 ka. The crater data indicate that class 2 craters are ~200 to 600 ka. We ascribe an age of 10–20 Ma to class 6 craters based on the crater retention age of small craters on Meridiani Planum. As a result, classes 3–5 craters must fall in between and we ascribe an age of ~0.6–2 Ma, ~2–4 Ma, and ~4–10 Ma to classes 3, 4, and 5 craters, respectively (Table 2).

6. Rate of Crater Modification

Simple hypervelocity fresh impact craters have a well-understood morphometry that varies little. They are typically bowl shaped with a depth/diameter ratio of 0.2 and a rim height/diameter ratio of about 0.04 [*Pike*, 1977; *Melosh*, 1989]. Small fresh lunar craters [*Basilevsky et al.*, 2014] and a sample of several hundred

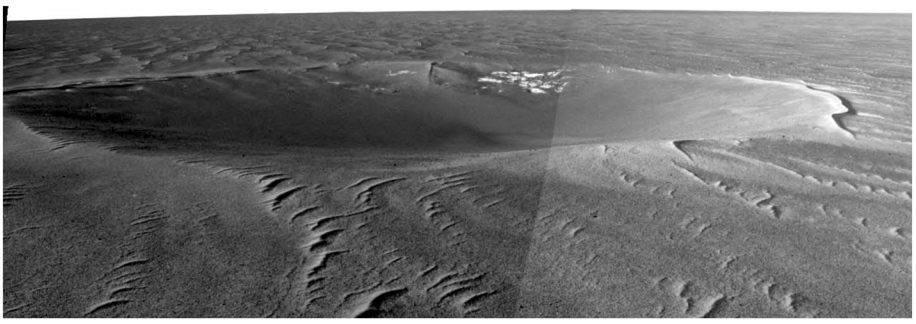

Figure 19. Navcam mosaic of class 5, Voskhod crater acquired on Sol 2441 when the rover was 7 m to the south. Note the planed off blocks and eroded rim overtaken by ripples and no ejecta.

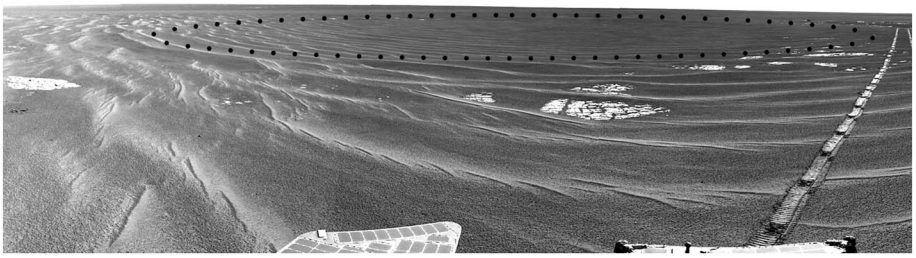

Figure 20. Navcam image of class 6 crater, Kitty Clyde's Sister, acquired on Sol 943 looking to the southwest. HiRISE image of crater is shown in Figure 17. Note planed off blocks that define the crater rim (black dots) and ripples throughout.

small primary craters observed in before and after images (Context Camera, CTX and HiRISE) of Mars also have depth/diameter ratios of about 0.2 [*Daubar and McEwen*, 2009; *Daubar et al*., 2014]. Secondary craters, if present, appear to have a depth/diameter ratio of about half (0.1) that of primary craters [*Pike and Wilhelms*, 1978]. However, none of the craters in the catalog have characteristics that would indicate they are secondaries and far-field secondaries, which would be harder to distinguish from

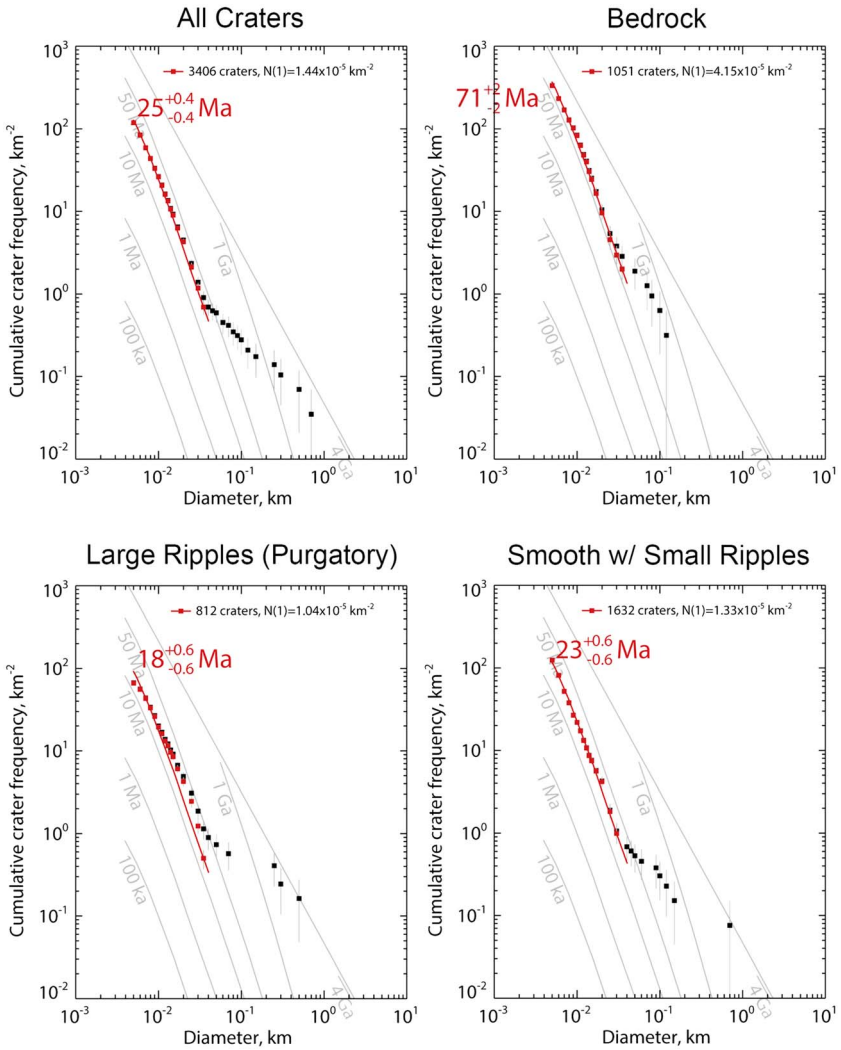

Figure 21. Cumulative number of craters versus diameter plots for craters around the *Opportunity* traverse measured in HiRISE for different terrains. Ages and uncertainties shown are fits for crater diameters indicated by the length of the line using incremental fits and applying a resurfacing correction using the method of *Michael and Neukum* [2010] and *Platz et al*. [2013] with isochrons from *Hartmann* [2005] as described in the text.

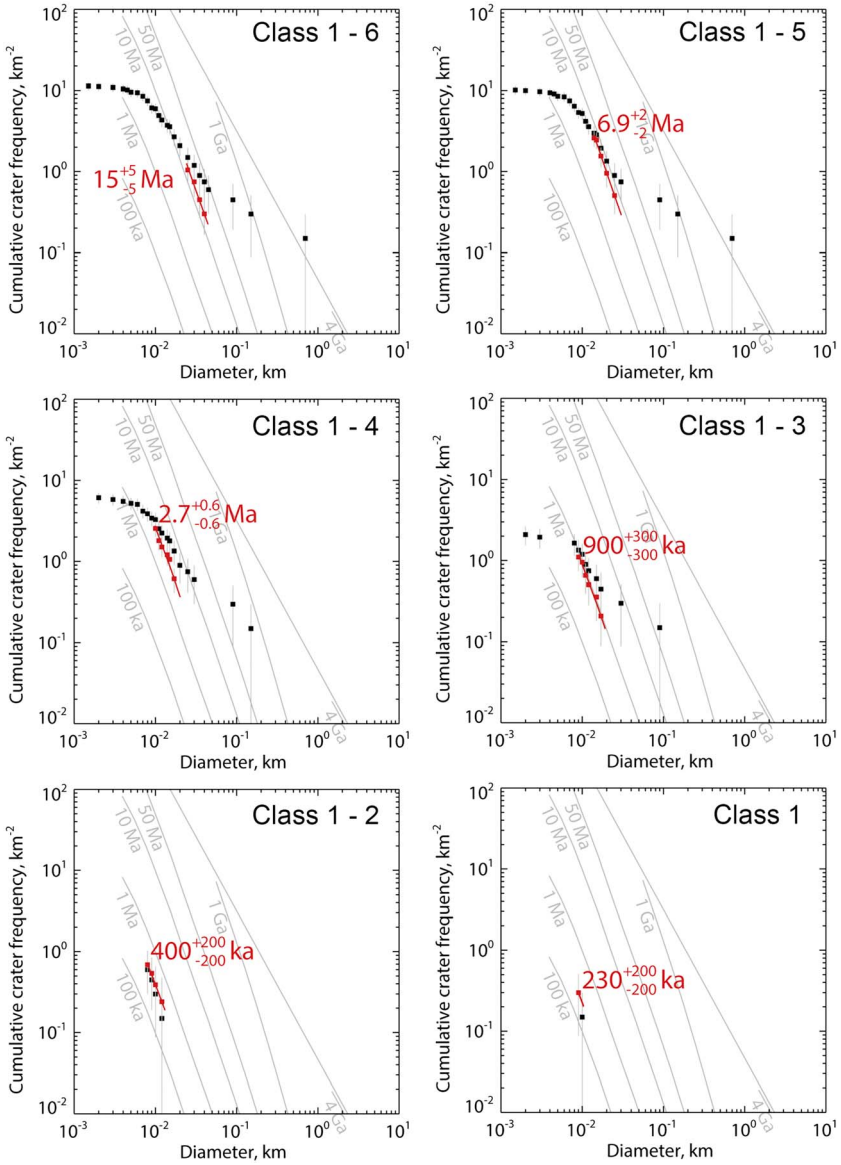

Figure 22. Cumulative number of craters versus diameter plots for craters in each morphological class and younger as imaged by the rover in all terrains. Ages and uncertainties shown are fits for crater diameters indicated by the length of the line using incremental fits and applying a resurfacing correction using the method of *Michael and Neukum* [2010] and *Platz et al*. [2013] with isochrons from *Hartmann* [2005] as described in the text.

primaries and thus more likely to be included in the catalog, have depth/diameter ratios that are similar to primaries [*Watters and Radford*, 2014]. *Melosh* [1989] reports a relationship between the maximum block ejected from a crater and its diameter, $B = KD^{2/3}$, where B, the block size, and D, crater diameter, are in meters and K is a constant. Data reported in *Moore* [1971] and *Bart and Melosh* [2007, 2010] suggest that K is typically 0.1 to 0.3 for primary lunar craters. These relations allow us to quantify the change in crater shape and ejecta block size and because we have ages for each morphologic class, we can determine the rate of degradation since they formed.

One measure of crater degradation comes from sediment deposition in the crater interior, which could result from either eolian sediment transport and/or backwasting of the crater walls. The rate of deposition of sand into a crater is determined by subtracting the observed crater depth from the original crater depth (0.2 times the diameter) and dividing by the age of the crater. We report this as the degradation rate in units of m/Myr in Table 1 (Tables S1a and S1b) for each crater (where degradation includes any modification

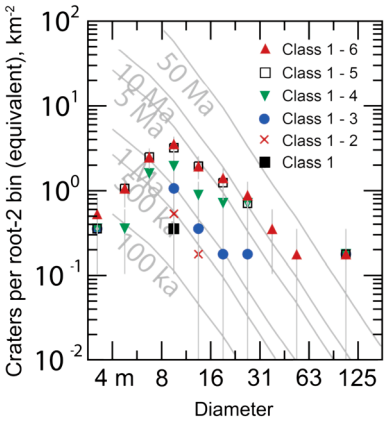

Figure 23. Incremental number of craters versus diameter plot for craters in each morphological class and younger in the catalog. Plot from craterstats [*Michael and Neukum*, 2010] with isochrons from *Hartmann* [2005].

of the crater). The unit m/Myr is conveniently equivalent to μm/yr, which is a Bubnoff unit commonly used in the terrestrial erosion rate literature [e.g., *Saunders and Young*, 1983]. Class 2 craters that formed ~200–500 ka have an average degradation rate of 0.9 m/Myr, for an assumed crater age of 400 ka. Class 3 craters that formed ~1–3 Ma have average degradation rates of 1.1 m/Myr, assuming a crater age of 2 Ma; Class 4 craters that formed around 2–4 Ma have an average degradation rate of ~0.4 m/Myr, assuming a crater age of 3 Ma. Class 5 craters that formed 4–10 Ma have an average degradation rate of ~0.2 m/Myr, for an assumed crater age of 7 Ma. Finally, class 6 craters that formed around 15 Ma also have a similar average degradation rate of ~0.2 m/Myr for craters. Larger craters have higher degradation rates by a factor of 2–5 than smaller craters, but it is also possible that these larger craters have survived beyond 20 Ma, which would reduce the degradation rate.

The rate of erosion of ejecta blocks is similar to the degradation rates based on the deposition of sand in crater interiors. Class 4 craters have ejecta blocks that are completely planed off. The majority of craters in this class are less than 10 m diameter and most are less than 20 m diameter. The largest ejecta blocks for 10–20 m diameter craters are roughly 0.5–2 m in size. We estimate that roughly 1 m of erosion would be needed to plane off blocks of this size, which results in an erosion rate of ~0.3 m/Myr for the past 3 Ma. Class 5 and 6 craters have no ejecta visible, so blocks must be planed off and covered with sand. Class 6 craters average 22 m diameter, so maximum block sizes are ~1.5 m. Assuming ~1.5 m of erosion is needed to plane off the blocks and cover them with sand results in erosion rates of 0.1 m/Myr for the past 15 Ma. These estimates of maximum block size and amount of erosion generally exceed calculated maximum ejecta thickness at the crater rims [*McGetchin et al*., 1973]. Using equations reported in *Grant et al*. [2008], near-rim ejecta thickness is roughly 0.1–0.8 m for 5–20 m diameter craters and so erosion to plane off the largest ejecta blocks could also erode away the ejecta.

The rate of erosion of crater rims is also similar to the degradation and erosion rates derived above. Class 5 and 6 craters do not have elevated rims, indicating they have been eroded away. Class 5 and 6 craters average 9 and 22 m diameter, so original rims were 0.4 and 0.9 m high, which yields erosion rates of ~0.05 and 0.06 m/Myr for the past 7 and 15 Ma, respectively. Because rims progressively degrade from class 1 to class 4 craters, the resulting average erosion rates from rimless class 5 and 6 craters are averages for the past 20 Myr.

Uncertainties in the calculated degradation rates are related to the accuracy of the morphometric measurements, the assumed initial geometry of the craters and ejecta, and the uncertainties in the age determinations. Measurements of depth and diameter are accurate within a few percent (section 3) and small hypervelocity impact craters have remarkably predictable initial geometries (section 6). Ejecta block size varies by a factor of 3 from the range in the constant K. Although measurement and model uncertainties for any individual crater could be large, we cite average rates of degradation for each class of craters. As a result, individual uncertainties are unlikely to affect the overall order of magnitude decrease in erosion rate that is observed. All of these uncertainties are dwarfed by uncertainties in the ages determined by matching crater size-frequency distributions to isochrons. Although the statistical uncertainty in the fit to model ages is relatively small (Figures 21 and 22), it is likely that derived ages could be uncertain by an order of magnitude. However, the relative age differences between the crater classes and thus the observed decrease in degradation rate should not be affected.

Relatively high erosion rates in the recent past at Meridiani Planum are likely due to the easily erodible sulfate sandstones, the abundant sand supply, and the evidence for recent mobility of sand. Sulfate sandstones of the Burns formation are weak and easily erodible based on the observed planing off of blocks parallel to the sand and ripple surface [*Grant et al*., 2006a; *Golombek et al*., 2006a] and observed specific grind energies needed to abrade them [*Arvidson et al*., 2004; *Thomson et al*., 2013]. The surface that *Opportunity* traversed is dominated by dark basaltic sand organized into granule ripples of various sizes [*Soderblom et al*., 2004].

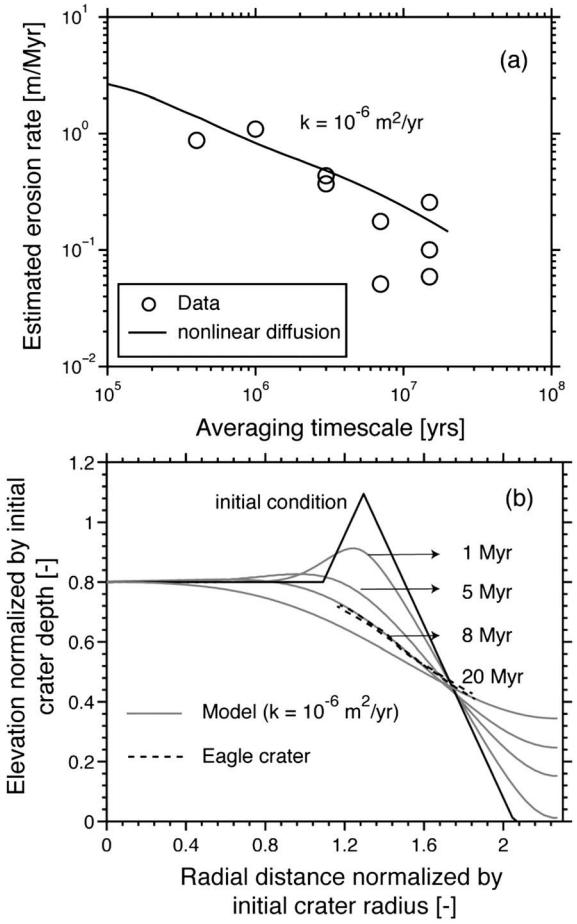

Figure 24. Results of radially symmetric topographic diffusion model [*Pelletier and Cline*, 2007] with a diffusivity (k) of 10^{-6} m^2/yr and a threshold slope of 35°. The initial condition for the model includes a 30° crater wall, with a depth of 20% and rim height of 4% of the crater diameter. The boundary conditions are zero slope at the center of the crater and zero slope and fixed elevation far away outside the crater. (a) Estimated erosion rate (calculated as the decrease in crater depth divided by time) from the model versus averaging timescale shows that decrease in erosion rate for small Meridiani craters can be explained as a result of the decrease in slope of crater walls with time. Data points are averages from crater infill, ejecta block, and rim erosion for different class craters on Meridiani as discussed in the text. (b) Plot showing temporal evolution of the crater profile where the radial distance is normalized by the crater radius and the elevation normalized by initial crater depth. With time, the crater rim rounds, the slope decreases, and the crater fills. Topographic profiles of Eagle crater (thick, dashed lines from *Grant el al.* [2006a]) show good agreement with the model results for a diffusivity of 10^{-6} m^2/yr.

Although the granule ripples have been inactive for the past ~50–200 ka, fine sand has been clearly moving around on Meridinai Planum. Concepción crater, which is younger than the latest phase of granule ripple migration [*Golombek et al.*, 2010], has had sand deposited into its interior and filled in around and eroded ejecta blocks. Fine sand has also been observed to fill old rover tracks [*Geissler et al.*, 2008, 2010], form recently active ripples on the floor of Eagle and Discovery craters [*Sullivan et al.*, 2005, 2007; *Jerolmack et al.*, 2006; *Golombek et al.*, 2010], and form younger cuspate and secondary ripples from winds funneled along the troughs [*Sullivan et al.*, 2007].

Our erosion rate estimates in the recent past at Meridiani are similar to previous estimates. Erosion rates as high as 1–10 m/Ma have been reported for the recent past on Mars. Erosion of ejecta blocks to liberate blueberries around Concepción crater has been estimated at about 1 m/Ma in the past 10 ka [*Golombek et al.*, 2010], and infill has been estimated at 10 m/Ma (section 7.1). Erosion and smoothing of boulders on a ~1 Ma inactive alluvial fan has been estimated at ~1 m/Myr [*de Haas et al.*, 2013]. Abrasion rates of 1–10 m/Myr have been estimated from measurements of the migration rate of sand ripples and dune lee fronts at the Nili Patera dune field [*Bridges et al.*, 2012]. Finally, young very lightly cratered layered deposits on Mars in general require erosion rates of roughly 1 m/Myr to be free of craters [*Malin and Edgett*, 2000; *McEwen et al.*, 2005] and *Grinrod and Warner* [2014] extend rates this high to 200–400 Ma for interior layered deposits in Valles Marineris.

7. Discussion: Erosion Rate Changes With Time

7.1. Meridiani Crater Erosion Rates

The rate of degradation (infill and erosion) calculated for different age craters shows a clear decrease with increasing age (Figure 24a). Classes 2 and 3 craters that formed in the past ~0.2–2 Ma have an average degradation rate of ~1 m/Myr. The erosion/degradation rate drops to 0.3–0.4 m/Myr for the past 3 Myr, 0.05–0.2 m/Myr for the past 7 Myr, and 0.06–0.3 m/Myr for the past 15 Myr. One class 1 crater, Concepción, has had around 1 m of sand deposited on its floor, suggesting a short-term degradation rate of ~10 m/Myr in the past 100 ka.

The simplest interpretation of the tenfold drop in degradation rate for craters on Meridiani from 1 Ma to 15 Ma is that it is due to local changes in sand supply, surface roughness, and the reduction of crater wall

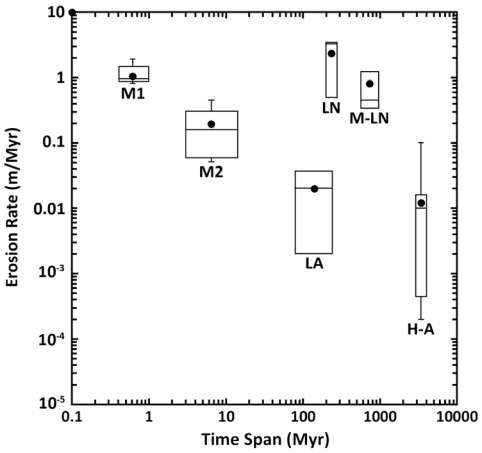

Figure 25. Box and whiskers plot of published erosion rates on Mars versus the time span over which the erosion rate is calculated. Box height delineates the middle two quartiles of the estimates around the median (line), with the whiskers showing the extrema and the dot showing the mean; time span of the rates in the box defines the width. Data point at 0.1 Myr is for degradation of Concepción crater (class 1) as described in the text and represents the maximum short-term rate in the modern era. Erosion rate marked M1 includes our classes 2 and 3 crater degradation rates at Meridiani Planum, plus erosion of an alluvial fan [*de Haas et al*., 2013], and lightly cratered layered terrain [*Malin and Edgett*, 2000; *McEwen et al*., 2005]. Erosion rates marked M2 are from our class 4–6 degradation rates for craters in Meridiani Planum. Erosion rates marked LA are Late Amazonian erosion rates from *Golombek et al*. [2006a] and *Farley et al*. [2014] (converted from scarp retreat to erosion rate of 3 m in 80 Myr). Erosion rates marked H-A are Hesperian through Amazonian rates from *Arvidson et al*. [1979], *Carr* [1992], *Golombek and Bridges* [2000], *Golombek et al*. [2006a, 2006b], *Grant et al*. [2006b], *Warner et al*. [2010], and *Newsom et al*. [2014]. Erosion rates marked M-LN are rates for the Middle through Late Noachian from *Craddock and Maxwell* [1993], *Craddock et al*. [1997], and *Hartmann et al*. [1999]. Erosion rates marked LN are for the Late Noachian from *Carr* [1992], *Hynek and Phillips* [2001], and *Warner et al*. [2010]. The time span for the erosion rates has been adjusted for changes to the ages of the Martian epochs reported in *Werner and Tanaka* [2011] for the *Hartmann* [2005] production function.

slopes as craters degrade after an impact. Immediately after an impact, ejecta with a wide variety of grain sizes including blocks are deposited on the surface out of equilibrium with the eolian regime. Sand-size grains produced or deposited on the surface by the impact are saltated by the wind, quickly eroding weak sulfate ejecta blocks in the wind stream, and are deposited in quiet areas around ejecta blocks and inside craters. For short periods, our results show that the rates of modification can be as high as 1–10 m/Myr, and then decrease with time as the crater degrades. Over millions of years, crater relief also decreases due to eolian infill, crater wall backwasting, mass failure, saltation abrasion, and disturbance-driven creep from microimpacts, saltating sand, and seismicity. All of these processes likely depend on crater relief and wall gradients, and therefore slow in time as craters degrade, crater relief decreases, and crater wall slopes shallow. *Basilevsky et al*. [2014] also report a slope decrease with time for comparably small lunar craters and a nonlinear degradation that slows with time. Finally, because our rate estimates are averages over the age of the crater class and initial rates are high, subsequent rates must be even lower than the average.

To show quantitatively that decreasing erosion rates with crater age can be explained by relaxation of crater relief in time, we model the topographic evolution of a crater using radially symmetric, nonlinear topographic diffusion [*Pelletier and Cline*, 2007]. Topographic diffusion should be a reasonable approximation of crater transport processes in which sediment flux increases with topographic slope, which is likely the case for mass wasting, disturbance-driven creep, and slope-directed eolian transport. We numerically solved the radially symmetric nonlinear diffusion equation where the initial condition is a 30° crater wall, a depth of 20% the crater diameter, and rim height of 4% of the crater diameter (Figure 24b) [*Pelletier and Cline*, 2007]. The boundary conditions are zero slope at the center of the crater and zero slope and fixed elevation at a location far away outside the crater. The threshold slope for mass wasting by gravity alone was set to 35°. Solutions of the diffusion equation depend only on the scarp slope, height, and the diffusivity, a term that characterizes the erodibility of the material and the vigor of erosion and downslope sediment transport. With time, the crater rim rounds, the slope decreases, and the crater fills. In the model, the average erosion rate also decreases in time (Figure 24a) because the crater walls relax, and sediment flux decreases with decreasing wall slopes. The modeled crater slope matches that observed for Eagle (10°, profiles from *Grant et al*. [2006a]) in 8 Myr (Figure 24b). The diffusivity (κ, using equation 2 of *Pelletier and Cline* [2007]), which best fits the observed decrease in the rate of erosion, is approximately 10^{-6} m^2/yr for Eagle crater (Figure 24a. These results argue that the decrease in erosion rate in Figure 24a can be explained simply by the reduction in topographic slopes as craters degrade with time.

Our diffusivity and erosion rate estimates are similar to values estimated for the Moon of 10^{-5}–10^{-6} m^2/yr, which corresponds to erosion rates of $0.2–0.5 \times 10^{-3}$ m/Myr [*Craddock and Howard*, 2000; *Fassett*, 2013; *Fassett and Combellick*, 2014]. In contrast, diffusivities on Earth derived from global compilations of slow, relatively

continuous mass movements [*Martin and Church*, 1997; *Saunders and Young*, 1983] indicate terrestrial values of 10^{-3} to 10^{-4} m^2/yr. Larger diffusivities on Earth are not surprising given that terrestrial diffusion in part incorporates precipitation, rock type, and biologic activity (e.g., vegetation cover), factors that either had no control over hillslope diffusion at Meridiani Planum (e.g., vegetation and precipitation) or were constant during the degradational process across the region (e.g., bedrock type). Nonetheless, these comparisons show that Mars degradational processes over the past 20 Ma at Meridiani Planum are 1–3 orders of magnitude slower than similar processes on Earth and similar to the desiccated and atmosphereless surface of the Moon.

7.2. Comparison to Longer-Term Rates in the Amazonian and Hesperian

Erosion rates calculated over longer timescales in the Amazonian and Hesperian are slower than what we estimated for the past 20 Myr at Meridiani Planum. For example, erosion rates averaged over 80–400 Myr (marked LA for Late Amazonian on Figure 25) are derived from the concentration of blueberries at the surface and the degradation of small craters at Meridiani Planum over the Late Amazonian [*Golombek et al*., 2006a], erosion of large (diameter >8 km) Hesperian craters [*Warner et al*., 2010], and from cosmic ray exposure ages at Gale crater [*Farley et al*., 2014] and are about an order of magnitude slower (~0.01 m/Myr) than those averaged over 10 Myr (M2 on Figure 25).

Erosion rates averaged over the ~3 Gyr from the deflation of the Mars Pathfinder landing site and the cratered plains at Gusev since the Hesperian are exceptionally slow ($2–3 \times 10^{-5}$ m/Myr) [*Golombek and Bridges*, 2000; *Golombek et al*., 2006b]. Slightly higher erosion rates (~10^{-3} m/Myr) have been estimated from the deflation of Husband Hill [*Grant et al*., 2006b] and the Viking 1 landings site [*Arvidson et al*., 1979]. Finally, erosion rates of ~0.01 m/Myr and higher have been estimated from the degradation of Hesperian and younger craters and crater populations by *Carr* [1992], *Warner et al*. [2010], and *Arvidson et al*. [1979] at the Viking Lander 2 site and *Newsom et al*. [2014] at Gale crater. The middle two quartiles of these erosion rates over ~3 Gyr are ~$0.5–15 \times 10^{-3}$ m/Myr (marked H-A for Hesperian through Amazonian on Figure 25). Because the means of the 100 Myr and 3 Gyr estimates are similar, we interpret these rates as being long-term averages for eolian erosion during the Hesperian and Amazonian.

The decrease in erosion rates as a function of measurement time interval over the past several billion years cannot be explained by simple topographic diffusion, as was the case for the small craters surveyed by *Opportunity*. Instead, over such long time spans the decrease in erosion rate with increasing time may be due to heavy-tailed hiatuses that separate the actual erosional events. For example, sediment accumulation rates have been shown to exhibit a negative power law dependence on the timescale of measurement due to periods of inactivity or hiatuses (sometimes referred to as timescale bias) [*Sadler*, 1981, 1999; *Pelletier*, 2007]. The similarity of average erosion rates since 3 Ga when measured over 100 Myr and 3 Gyr together with the long spatiotemporal scales of averaging involved in these estimates argue that they are representative of the true long-term process rate that includes the hiatuses [*von Hagke et al*., 2014].

Comparing Hesperian through Amazonian erosion rates to a compilation of erosion rates on Earth calculated over similar timescales [*von Hagke et al*., 2014] shows that the erosion rates on Mars during the Amazonian and Hesparian are 3–4 orders of magnitude slower, consistent with the diffusivity comparisons in section 7.1 and confirm that recent Martian surface processes are dramatically slower than on Earth. Note that the calculated erosion rates at Meridiani are slow despite the observations of mechanically weak sulfate sandstones, which further underscores the highly inactive or inefficient erosional processes as compared to Earth. As a result, recent Martian rates are likely too slow for liquid water to be an important erosional agent, which suggests that erosion in the Hesperian and Amazonian on Mars instead has been due to slow eolian erosion in a dry and desiccating environment.

7.3. Comparison to Longer-Term Erosion Rates During the Noachian

Higher erosion rates on Mars (around 1 m/Myr) have been reported for the Middle to Late Noachian based on crater size-frequency distributions [*Craddock and Maxwell*, 1993; *Craddock et al*., 1997; *Carr*, 1992; *Hynek and Phillips*, 2001; *Hartmann et al*., 1999; *Warner et al*., 2010] and erosion of Meridiani during Late Noachian valley network formation [*Hynek and Phillips*, 2001]. Shorter timescale estimates (200–300 Myr) during this period may be about 3 times faster than longer estimates over 500 Myr to 1 Gyr (Figure 25, marked M-LN for Middle through Late Noachian and LN for Late Noachian), although the data overlap so they may not be

different. We argue that these Noachian rates represent true long-term process rates that include hiatuses for two reasons. First, the entire period of high erosion rates only occurred over this relatively short period of Martian history, so longer-term rates are not applicable. Second, landscapes dominated by fluvial erosion on Earth have been shown to have relatively short hiatuses that can be averaged out over centuries to thousands of years to derive true long-term process rates [*von Hagke et al*., 2014].

These Noachian rates of erosion are 2–3 orders of magnitude faster than Hesperian through Amazonian rates and are similar to typical slow continental erosion rates on Earth that are dominated by liquid water [*Saunders and Young*, 1983; *Judson and Ritter*, 1964; *Portenga and Bierman*, 2011] and are comparable to long-term erosion rates over similar timescales on Earth [*von Hagke et al*., 2014]. Short-term erosion rates over Myr timescales during this period could be several orders of magnitude faster and thus similar to fast short-term erosion rates on Earth [e.g., *Bierman and Nichols*, 2004; *Portenga and Bierman*, 2011]. Diffusivities for crater degradation and alluvial fan development for the wetter Late Noachian to Early Hesperian on Mars also have assumed a more broad range of terrestrial-like values of 10^{-1} to 10^{-4} m^2/yr [*Howard*, 2007; *Forsberg-Taylor et al*., 2004; *Armitage et al*., 2011], values much larger than what we estimate for Meridiani Planum in the last 20 Ma. The similarity between Noachian and terrestrial rates argues that Late Noachian erosion on Mars was also dominated by liquid water and that a more clement climate existed at that time. The decrease in erosion rate data suggests that the change in climate occurred after the Late Noachian or Early Hesperian on Mars.

8. Summary and Conclusions

Opportunity traversed 33.5 km across Meridiani Planum from Eagle to Endeavour craters across surfaces that are: smooth and sandy, composed of medium and large granule ripples, and beveled flat outcrop of sulfate sandstones of the Burns formation. In addition to navigating to Endurance and Victoria craters to study outcrop exposures, the path was planned to avoid large eolian bed forms of fine sand similar to the one at Purgatory ripple where the rover became embedded and to investigate smaller craters along the route. About 100 craters were imaged by *Opportunity* by either targeting them in advance along the route (e.g., Resolution cluster, Concepción, and Santa Maria craters) or as targets of *Opportunity* at the end of drives or as "drive by shootings" in the middle of a drive.

We created a catalog of the morphometry (depth and diameter) and morphology (interior, rim, and ejecta) of ~100 small (<200 m diameter) craters imaged by the *Opportunity* rover during the traverse (most craters are <20 m diameter). The frequency of craters varies from approximately one crater per kilometer of traverse in areas with large granule ripples to approximately five craters per kilometer of traverse on smooth terrain with very small ripples, suggesting that eolian activity associated with large ripples degrades craters faster than that on smooth sandy surfaces, possibly due to more abundant sand. In HiRISE, the smooth terrain exhibits over a factor of 2 higher crater density (in number of craters/km^2) relative to regions with larger ripples.

Six morphologic states with increasing degradation are recognized. Class 1 craters have elevated rims, blocky inner walls, rims, and ejecta, and they are superposed on the granule ripples. Class 2 craters have elevated rims, partially planed off ejecta blocks and inner walls, sandy interiors, and ripples that merge with their rims. Class 3 craters have elevated rounded rims, mostly planed off blocky ejecta, blocky inner walls, and shallow sandy floors and ripples that merge with their rims. Class 4 craters have slightly elevated rims, shallow sandy interiors, completely planed off ejecta blocks, and ripples that modify their rims. Class 5 craters are mostly sandy depressions, with flat rims, no ejecta and ripples that merge with and follow the edge of the crater. Class 6 craters are rimless, very shallow, mostly sandy depressions, with no ejecta and pervasive ripples.

The age of each morphologic class of crater has been determined from crater size-frequency distributions of craters in the catalog, the crater retention age of small craters on Meridiani Planum, and their age with respect to the latest phase of granule ripple migration. Class 1 craters are younger than the latest phase of granule ripple migration and are therefore <50–200 ka. Class 2 craters are older than the latest phase of granule ripple migration and thus ~200–600 ka. Class 3–5 craters are ~0.6–2 Ma, ~2–4 Ma, and ~4–10 Ma, respectively. Finally, class 6 craters are about ~10–20 Ma based on the crater retention age of small craters on Meridiani Planum.

The rate of crater degradation is determined by comparing its depth, ejecta block size, and rim height, with that expected for a fresh hypervelocity impact crater and dividing by its age. The rate of deposition of sand into

craters drops from ~1 m/Myr for craters ~1 Ma to ~0.2 m/Ma for craters 8–10 Ma. The rate of erosion of ejecta blocks drops from ~0.3 m/Myr for craters ~3 Ma to 0.1 m/Myr for craters ~15 Ma. Finally, the rate of erosion of crater rims is ~0.05 for classes 5 and 6 craters that are ~7–15 Ma. As a result, the rate of degradation of craters decreases by an order of magnitude from ~1 Ma to 20 Ma.

This order of magnitude decrease in erosion rate is consistent with the simple reduction in scarp slope via downslope transport of material, which has been modeled by numerically solving a form of the nonlinear, radially symmetric diffusion equation that depends only on the scarp slope, height, and the diffusivity, a term that characterizes the erodibility of the material and the vigor of the downslope motion. The decrease in inner crater wall slope for observed topographic profiles of Eagle crater from initial slopes of ~30° over its estimated age can be well fit by the diffusion model for calculated diffusivities of ~10^{-6} m^2/yr.

Erosion rates of ~1–10 m/Myr reported in the literature for Meridiani, inactive alluvial fans, crater free layered deposits, and the migration rate of bed forms are likely peak short-term eolian erosion rates in the modern Martian environment. In contrast, mean erosion rates averaged over 80–400 Myr are several orders of magnitude slower (~0.01 m/Myr) and are similar to mean erosion rates averaged over 3 Gyr determined mostly from deflation of the landing sites. We interpret these rates as being long-term averages for eolian erosion during the Hesperian and Amazonian. These rates are 3–4 orders of magnitude slower than typical erosion rates on Earth calculated over similar timescales in which liquid water is the erosional agent. Slow eolian erosion is also indicated by the derived diffusivities from the reduction in crater wall slopes that are 2–3 orders of magnitude lower than similar diffusivities on Earth and similar to lunar diffusivities.

Higher erosion rates (~1 m/Myr) on Mars have been reported in the literature for the Middle to Late Noachian based on crater size-frequency distributions and erosion of Meridiani during Late Noachian valley network formation. These Noachian rates probably represent true long-term process rates that include hiatuses because they occur over relatively short periods of Martian history and landscapes dominated by fluvial erosion on Earth have been shown to have relatively short hiatuses that can be averaged out over centuries to thousands of years. These Noachian rates of erosion are 2–3 orders of magnitude faster than Amazonian rates and are similar to typical continental erosion rates on Earth calculated over similar timescales. This similarity argues that Late Noachian erosion on Mars was also dominated by liquid water and that a wetter climate existed at that time.

Acknowledgments
Research described in this paper was carried out by the Mars Exploration Rover Project, Jet Propulsion Laboratory, California Institute of Technology, under a contract with NASA. All data from the Opportunity rover and HiRISE are available from the NASA Planetary Data System. N. Warner was supported by the NASA Postdoctoral Program. M. Lamb was supported by NASA grant NNX13AM83G. V. Ganti was supported by NSF NCED2 program. We thank Brad Jolliff for help with the crater catalog, John Grant for data on Eagle, Endurance, Victoria, and Santa Maria craters, Jane Willenbring for discussions on timescale bias in erosion rates, C. Fassett, T. Platz, R. Anderson, and P. Geissler for reviews, and V. Carranza, C. Schwartz, and E. Bondi for help with the figures.

References

Armitage, J. J., N. H. Warner, K. Goddard, and S. Gupta (2011), Timescales of alluvial fan development by precipitation on Mars, *Geophys. Res. Lett.*, *38*, L17203, doi:10.1029/2011GL048907.

Arvidson, R., E. Guiness, and S. Lee (1979), Differential aeolian redistribution rates on Mars, *Nature*, *278*, 533–535.

Arvidson, R. E., et al. (2004), Localization and physical properties experiments conducted by Opportunity at Meridiani Planum, *Science*, *306*, 1730–1733, doi:10.1126/science.1104211.

Arvidson, R. E., et al. (2006), Nature and origin of the hematite-bearing plains of Terra Meridiani based on analyses of orbital and Mars Exploration Rover data sets, *J. Geophys. Res.*, *111*, E12S08, doi:10.1029/2006JE002728.

Arvidson, R. E., et al. (2011), Opportunity Mars Rover mission: Overview and selected results from Purgatory ripple to traverses to Endeavour crater, *J. Geophys. Res.*, *116*, E00F15, doi:10.1029/2010JE003746.

Arvidson, R. E., et al. (2014), Ancient aqueous environments at Endeavour crater, Mars, *Science*, *343*, doi:10.1126/science.1248097.

Bart, G. D., and H. J. Melosh (2007), Using lunar boulders to distinguish primary from distant secondary impact craters, *Geophys. Res. Lett.*, *34*, L07203, doi:10.1029/2007GL029306.

Bart, G. D., and H. J. Melosh (2010), Distributions of boulders ejected from lunar craters, *Icarus*, *209*, 337–357, doi:10.1016/j.icarus.2010.05.023.

Basilevsky, A. T., M. A. Kreslavsky, I. Karachevtseva, and E. N. Gusakova (2014), Morphometry of small impact craters in the Lunokhod-1 and Lunokhod-2 study areas, *Planet. Space Sci.*, *92*, 77–87, doi:10.1016/j.pss.2013.12.016.

Bierman, P., and K. Nichols (2004), Rock to sediment-slope to sea with ^{10}Be-rates of landscape change, *Annu. Rev. Earth Planet. Sci.*, *32*, 215–255.

Bridges, N. T., F. Ayoub, J. P. Avouac, S. Leprince, A. Lucas, and S. Mattson (2012), Earth-like sand fluxes on Mars, *Nature*, *485*, 339–342, doi:10.1038/nature11022.

Carr, M. H. (1992), Post-Noachian erosion rates: Implications for Mars climate change, *Lunar Planet. Sci.*, *23*, 205–206.

Christensen, P. R., et al. (2004), The Thermal Emission Imaging System (THEMIS) for the Mars 2001 Odyssey mission, *Space Sci. Rev.*, *110*, 85–130.

Craddock, R. A., and A. D. Howard (2000), Simulated degradation of lunar impact craters and a new method for age dating farside mare deposits, *J. Geophys. Res.*, *105*(E8), 20,387–20,401, doi:10.1029/1999JE001099.

Craddock, R. A., and T. A. Maxwell (1993), Geomorphic evolution of the Martian highlands through ancient fluvial processes, *J. Geophys. Res.*, *98*, 3453–3468, doi:10.1029/92JE02508.

Craddock, R. A., T. A. Maxwell, and A. D. Howard (1997), Crater morphology and modification in the Sinus Sabaeus and Margaritifer Sinus regions of Mars, *J. Geophys. Res.*, *102*, 13,321–13,340, doi:10.1029/97JE01084.

Daubar, I. J., and A. S. McEwen (2009), Depth to diameter ratios of recent primary impact craters on Mars, Lunar Planet. Inst. Sci. Conf. 40, abstract 2419.

Daubar, I. J., A. S. McEwen, S. Byrne, M. R. Kennedy, and B. Ivanov (2013), The current Martian cratering rate, *Icarus*, *225*, 506–516, doi:10.1016/j.icarus.2013.04.009.

Daubar, I. J., C. Atwood-Stone, S. Byrne, A. S. McEwen, and P. S. Russell (2014), The morphology of fresh craters on Mars and the Moon, *J. Geophys. Res. Planets*, doi:10.1002/2014JE004671.
de Haas, T., E. Hauber, and M. G. Kleinhans (2013), Local late Amazonian boulder breakdown and denudation rate on Mars, *Geophys. Res. Lett.*, *40*, 3527–3531, doi:10.1002/grl.50726.
Edwards, C. S., K. J. Nowicki, P. R. Christensen, J. Hill, N. Gorelick, and K. Murray (2012), Mosaicking of global planetary image datasets: 1 Techniques and data processing for Thermal Emission Imaging System (THEMIS) multi-spectral data, *J. Geophys. Res.*, *116*, E10008, doi:10.1029/2010JE003755.
Farley, K., et al. (2014), In situ radiometric and exposure age dating of the Martian surface, *Science*, *343*(6169), doi:10.1126/science.1247166.
Fassett, C. I. (2013), Crater degradation of kilometer-sized craters on the lunar maria: Initial observations and modeling, Lunar Planet. Sci. Conf. 44, abstract 2026.
Fassett, C. I., and J. R. Combellick (2014), The rate of crater degradation and topographic evolution on the Moon: Results from the maria and initial comparisons with the highlands, Lunar Planet. Sci. Conf. 45, Abstract 1429.
Fergason, R. L., P. R. Christensen, and H. H. Kieffer (2006), High-resolution thermal inertia derived from the Thermal Emission Imaging System (THEMIS): Thermal model and applications, *J. Geophys. Res.*, *111*, E12004, doi:10.1029/2006JE002735.
Forsberg-Taylor, N. K., A. D. Howard, and R. A. Craddock (2004), Crater degradation in the Martian highlands: Morphometric analysis of the Sinus Sabaeus region and simulation modeling suggest fluvial processes, *J. Geophys. Res.*, *109*, E05002, doi:10.1029/2004JE002242.
Geissler, P. E., et al. (2008), First in situ investigation of a dark wind streak on Mars, *J. Geophys. Res.*, *113*, E12S31, doi:10.1029/2008JE003102.
Geissler, P. E., R. Sullivan, M. Golombek, J. R. Johnson, K. Herkenhoff, N. Bridges, A. Vaughan, J. Maki, T. Parker, and J. Bell (2010), Gone with the wind: Eolian erasure of the Mars rover tracks, *J. Geophys. Res.*, *115*, E00F11, doi:10.1029/2010JE003674.
Golombek, M. P. (2012), Timescale of small crater modification on Meridiani Planum, Mars, 43rd Lunar Planet. Sci. Conf., Abstract 2267.
Golombek, M. P., and N. T. Bridges (2000), Erosion rates on Mars and implications for climate change: Constraints from the Pathfinder landing site, *J. Geophys. Res.*, *105*, 1841–1853, doi:10.1029/1999JE001043.
Golombek, M. P., et al. (2003), Selection of the Mars Exploration Rover landing sites, *J. Geophys. Res.*, *108*(E12), 8072, doi:10.1029/2003JE002074.
Golombek, M. P., et al. (2005), Assessment of Mars Exploration Rover landing site predictions, *Nature*, *436*, 44–48, doi:10.1038/nature03600.
Golombek, M. P., et al. (2006a), Erosion rates at the Mars Exploration Rover landing sites and long-term climate change on Mars, *J. Geophys. Res.*, *111*, E12S10, doi:10.1029/2006JE002754.
Golombek, M. P., et al. (2006b), Geology of the Gusev cratered plains from the Spirit rover transverse, *J. Geophys. Res.*, *111*, E02S07, doi:10.1029/2005JE002503.
Golombek, M., K. Robinson, A. McEwen, N. Bridges, B. Ivanov, L. Tornabene, and R. Sullivan (2010), Constraints on ripple migration at Meridiani Planum from Opportunity and HiRISE observations of fresh craters, *J. Geophys. Res.*, *115*, E00F08, doi:10.1029/2010JE003628.
Grant, J. A., et al. (2006a), Crater gradation in Gusev crater and Meridiani Planum, Mars, *J. Geophys. Res.*, *111*, E02S08, doi:10.1029/2005JE002465.
Grant, J. A., S. A. Wilson, S. W. Ruff, M. P. Golombek, and D. L. Koestler (2006b), Distribution of rocks on the Gusev Plains and on Husband Hill, Mars, *Geophys. Res. Lett.*, *33*, L16202, doi:10.1029/2006GL026964.
Grant, J. A., S. A. Wilson, B. A. Cohen, M. P. Golombek, P. E. Geissler, R. J. Sullivan, R. L. Kirk, and T. J. Parker (2008), Degradation of Victoria crater, Mars, *J. Geophys. Res.*, *113*, E11010, doi:10.1029/2008JE003155.
Grinrod, P. M., and N. H. Warner (2014), Erosion rate and previous extent of interior layered deposits on Mars revealed by obstructed landslides, *Geology*, *42*, 795–798, doi:10.1130/G35790.1.
Hartmann, W. (2005), Martian cratering 8: Isochron refinement and the chronology of Mars, *Icarus*, *174*, 294–320, doi:10.1016/j.icarus.2004.11.023.
Hartmann, W., and G. Neukum (2001), Cratering chronology and evolution of Mars, *Space Sci. Rev.*, *96*, 164–194.
Hartmann, W. K., M. Malin, A. McEwen, M. Carr, L. Soderblom, P. Thomas, E. Danielson, P. James, and J. Veverka (1999), Evidence for recent volcanism on Mars from crater counts, *Nature*, *397*, 586–589.
Herkenhoff, K. E., et al. (2004), Evidence from Opportunity's Microscopic Imager for water on Meridiani Planum, *Science*, *306*, 1727–1730.
Howard, A. D. (2007), Simulating the development of Martian highland landscapes through the interaction of impact cratering, fluvial erosion, and variable hydrologic forcing, *Geomorphology*, *91*, 332–363, doi:10.1016/j.geomorph.2007.04.017.
Hynek, B. M., and R. J. Phillips (2001), Evidence for extensive denudation of the Martian highlands, *Geology*, *29*, 407–410.
Hynek, B. M., R. E. Arvidson, and R. J. Phillips (2002), Geologic setting and origin of Terra Meridiani hematite deposit on Mars, *J. Geophys. Res.*, *107*(E10), 5088, doi:10.1029/2002JE001891.
Ivanov, B. (2001), Mars/Moon cratering rate ratio estimates, *Space Sci. Rev.*, *96*, 87–104.
Ivanov, B., H. J. Melosh, A. S. McEwen, and HiRISE Team (2008), Small impact crater clusters in high resolution HiRISE images, Lunar Planet. Sci., XXXIX, Abstract 1221.
Ivanov, B., H. J. Melosh, A. S. McEwen, and HiRISE Team (2009), Small impact crater clusters in high resolution HiRISE images II, Lunar Planet. Sci. XL, Abstract 1410.
Jakosky, B. M. (1979), The effects of nonideal surfaces on the derived thermal properties of Mars, *J. Geophys. Res.*, *84*(B14), 8252–8262, doi:10.1029/JB084iB14p08252.
Jerolmack, D. J., D. Mohrig, J. P. Grotzinger, D. A. Fike, and W. A. Watters (2006), Spatial grain size sorting in eolian ripples and estimation of wind conditions on planetary surfaces: Application to Meridiani Planum, Mars, *J. Geophys. Res.*, *111*, E12S02, doi:10.1029/2005JE002544.
Judson, S., and D. F. Ritter (1964), Rates of regional denudation in the United States, *J. Geophys. Res.*, *69*, 3395–3401, doi:10.1029/JZ069i016p03395.
Kieffer, H. H., S. C. Chase Jr., E. Miner, G. Münch, and G. Neugebauer (1973), Preliminary report on infrared radiometric measurements from the Mariner 9 spacecraft, *J. Geophys. Res.*, *78*(20), 4291–4312, doi:10.1029/JB078i020p04291.
Kieffer, H. H., T. Z. Martin, A. R. Peterfreund, B. M. Jakosky, E. D. Miner, and F. D. Palluconi (1977), Thermal and albedo mapping of Mars during the Viking primary mission, *J. Geophys. Res.*, *82*(28), 4249–4291, doi:10.1029/JS082i028p04249.
Lane, M. D., P. R. Christensen, and W. K. Hartmann (2003), Utilization of the THEMIS visible and infrared imaging data for crater population studies of the Meridiani Planum landing site, *Geophys. Res. Lett.*, *30*(14), 1770, doi:10.1029/2003GL017183.
Maki, J. N., et al. (2003), Mars Exploration Rover Engineering Cameras, *J. Geophys. Res.*, *108*(E12), 8071, doi:10.1029/2003JE002077.
Malin, M. C., and K. S. Edgett (2000), Sedimentary rocks of early Mars, *Science*, *290*, 1927–1937.
Malin, M. C., K. S. Edgett, B. A. Cantor, M. A. Caplinger, G. E. Danielson, E. H. Jensen, M. A. Ravine, J. L. Sandoval, and K. D. Supulver (2010), An overview of the 1985–2006 Mars Orbiter Camera science investigation, *Mars*, *5*, 1–60, doi:10.1555/mars.2010.0001.

Martin, Y., and M. Church (1997), Diffusion in landscape development models: On the nature of basic transport relations, *Earth Surf. Processes Landforms*, *22*, 273–279.
McEwen, A. S., B. S. Preblich, E. P. Turtle, N. A. Artemieva, M. P. Golombek, M. Hurst, R. L. Kirk, D. M. Burr, and P. R. Christensen (2005), The rayed crater Zunil and interpretations of small impact craters on Mars, *Icarus*, *176*, 351–381, doi:10.1016/j.icarus.2005.02.009.
McEwen, A. S., et al. (2010), The High Resolution Imaging Science Experiment (HiRISE) during MRO's Primary Science Phase (PSP), *Icarus*, *205*, 2–37, doi:10.1016/j.icarus.2009.04.023.
McGetchin, T. R., M. Settle, and J. W. Head (1973), Radial thickness variation in impact crater ejecta: Implications for lunar basin deposits, *Earth Planet. Sci. Lett.*, *20*, 226–236, doi:10.1016/0012-821X(73)90162-3.
Melosh, H. J. (1989), *Impact Cratering: A Geologic Process*, Oxford Univ. Press, New York.
Michael, G. G., and G. Neukum (2010), Planetary surface dating from crater size-frequency distribution measurements: Partial resurfacing events and statistical age uncertainty, *Earth Planet. Sci. Lett.*, *294*, 223–229, doi:10.1016/j.epsl.2009.12.041.
Moore, H. J. (1971), Large blocks around lunar craters, in *Analysis of Apollo 10 Photography and Visual Observations*, *NASA Spec. Publ.*, vol. SP-232, pp. 26–27, U.S. Gov. Print. Off., Washington, D. C.
Newsom, H. E., M. C. Palucis, L. C. Kah, N. Mangold, J. M. Williams, R. E. Arvidson, N. Stein, J. A. Grant, N. T. Bridges, and R. C. Wiens (2014), Resurfacing rates and erosion processes for Yellowknife Bay and the hummocky plains in Gale crater, Eight Int. Mars Conf., Abstract 1304.
Palluconi, F. D., and H. H. Kieffer (1981), Thermal inertia mapping of Mars from 60°S to 60°N, *Icarus*, *45*, 415–426.
Parker, T. J., M. P. Golombek, and M. W. Powell (2010), Geomorphic/geologic mapping, localization, and traverse planning at the Opportunity landing site, Mars, Lunar Planet. Sci. XLI, Abstract 2638.
Parker, T. J., F. J. Calef, M. P. Golombek, and T. M. Hare (2012), High-resolution basemaps for localization, mission planning, and geologic mapping at Meridiani Planum and Gale crater, 43rd Lunar Planet. Sci. Conf., Abstract 2535.
Pelletier, J. D. (2007), Cantor set model of eolian dust deposits on desert alluvial fan terraces, *Geology*, *35*, 439–442, doi:10.1130/G23367A.1.
Pelletier, J. D., and M. L. Cline (2007), Nonlinear slope-dependent sediment transport in cinder cone evolution, *Geology*, *35*, 1067–1070, doi:10.1130/G23992A.1.
Pike, R. J. (1977), Size-dependence in the shape of fresh impact craters on the Moon, in *Impact and Explosion Cratering*, edited by D. J. Roddy and R. B. Merrill, pp. 489–509 , Pergamon, New York.
Pike, R. J., and D. E. Wilhelms (1978), Secondary-impact craters on the Moon: Topographic form and geologic process, Lunar Planet. Sci. Conf. 9th, 907–909.
Platz, T., G. Michael, K. L. Tanaka, J. A. Skinner Jr., and C. M. Fortezzo (2013), Crater-based dating of geological units on Mars: Methods and application for the new global geological map, *Icarus*, *225*, 806–827, doi:10.1016/j.icarus.2013.04.021.
Portenga, E. W., and P. R. Bierman (2011), Understanding Earth's eroding surface with ^{10}Be, *Geol. Soc. Am. Today*, *21*(8), 4–10, doi:10.1130/G111A.1.
Powell, M. W., T. M. Crockett, J. S. Norris, and K. S. Shams (2010), Geologic mapping in Mars Rover operations, paper presented at Space-Ops Conference, Am. Inst. of Aeronaut. and Astronaut., Huntsville, Ala., 25–30 Apr.
Sadler, P. M. (1981), Sediment accumulation rates and the completeness of stratigraphic sections, *J. Geol.*, *89*, 569–584.
Sadler, P. M. (1999), The influence of hiatuses on sediment accumulation rates, in *On the Determination of Sediment Accumulation Rates*, GeoResearch Forum, vol. 5, edited by P. Bruns and H. C. Haas, pp. 15–40, Trans. Tech. Pub., Switzerland.
Saunders, I., and A. Young (1983), Rates of surface processes on slopes, slope retreat and denudation, *Earth Surf. Processes Landforms*, *8*, 473–501.
Soderblom, L. A., et al. (2004), Soils of Eagle crater and Meridiani Planum at the Opportunity rover landing site, *Science*, *306*(5702), 1723–1726, doi:10.1126/science.1105127.
Squyres, S. W., et al. (2006), Overview of the Opportunity Mars Exploration Rover Mission to Meridiani Planum: Eagle crater to Purgatory ripple, *J. Geophys. Res.*, *111*, E12S12, doi:10.1029/2006JE002771.
Squyres, S. W., et al. (2012), Ancient impact and aqueous processes at Endeavour crater, Mars, *Science*, *336*, 570–576, doi:10.1126/science.1220476.
Sullivan, R., et al. (2005), Aeolian processes at the Mars Exploration Rover Meridiani Planum landing site, *Nature*, *436*, 58–61, doi:10.1038/nature03641.
Sullivan, R., et al. (2007), Aeolian geomorphology with MER Opportunity at Meridiani Planum, Mars, Lunar Planet. Sci., XXXVIII, Abstract 2048.
Sullivan, R., R. Anderson, J. Biesiadecki, T. Bond, and H. Stewart (2011), Cohesions, friction angles, and other physical properties of Martian regolith from Mars Exploration Rover wheel trenches and wheel scuffs, *J. Geophys. Res.*, *116*, E02006, doi:10.1029/2010JE003625.
Thomson, B. J., N. T. Bridges, J. Cohen, J. A. Hurowitz, A. Lennon, G. Paulsen, and K. Zacny (2013), Estimating rock compressive strength from Rock Abrasion Tool (RAT) grinds, *J. Geophys. Res. Planets*, *118*, 1233–1244, doi:10.1002/jgre.20061.
Von Hagke, C., V. Ganti, D. Scherler, M. P. Lamb, W. W. Fischer, and J.-P. Avouac (2014), Climatic variability results in the persistence of transience in estimated erosion rates over millennial to million year timescales, Geophys. Res. Abs., 16, EGU2014-9160, EGU General Assembly.
Warner, N., S. Gupta, S.-Y. Lin, J.-R. Kim, J.-P. Muller, and J. Morley (2010), Late Noachian to Hesperian climate change on Mars: Evidence of episodic warming from transient crater lakes near Ares Vallis, *J. Geophys. Res.*, *115*, E06013, doi:10.1029/2009JE003522.
Watters, W. A., and A. C. Radford (2014), 3-D morphometry of Martian secondary impact craters from Zunil and Gratteri, 45th Lunar Planet. Sci. Conf., abstract 2836.
Weitz, C. M., R. C. Anderson, J. F. Bell III, W. H. Farrand, K. E. Herkenhoff, J. R. Johnson, B. L. Jolliff, R. V. Morris, S. W. Squyres, and R. J. Sullivan (2006), Soil grain analyses at Meridiani Planum, Mars, *J. Geophys. Res.*, *111*, E12S04, doi:10.1029/2005JE002541.
Werner, S. C., and K. L. Tanaka (2011), Redefinition of the crater-density and absolute-age boundaries for the chronostratigraphic system of Mars, *Icarus*, *215*, 603–607, doi:10.1016/j.icarus.2011.07.024.
Wray, J. J., E. Z. Noe Dobrea, R. E. Arvidson, S. M. Wiseman, S. W. Squyres, A. S. McEwen, J. F. Mustard, and S. L. Murchie (2009), Phyllosilicates and sulfates at Endeavour crater, Meridiani Planum, Mars, *Geophys. Res. Lett.*, *36*, L21201, doi:10.1029/2009GL040734.